NTNU – Trondheim
Norwegian University of
Science and Technology

The Effect of Thermophoresis on the Particle Deposition on a Cylinder

Henrik Fahre Lutro

Master of Science in Physics and Mathematics
Submission date: June 2012
Supervisor: Jon Andreas Støvneng, IFY
Co-supervisor: Nils Erland Haugen, SINTEF Energi AS

Norwegian University of Science and Technology
Department of Physics

NTNU
Faculty of Natural Sciences
and Technology
Department of Physics

MASTER THESIS

HENRIK FAHRE LUTRO

"The Effect of Thermophoresis on the Particle Deposition on a Cylinder"

Supervisors: Nils Erland L. Haugen
& Jon Andreas Støvneng

June 2012

Abstract

The effect of thermophoresis on the particle deposition on a cooled cylinder in non-isothermal laminar gas flow has been studied using Direct Numerical Simulations (DNS). Simulations where thermophoresis have been taken into account for different Stokes numbers and particle-to-gas thermal conductivity ratios, Λ, have been performed at Reynolds number $\mathrm{Re} = 380$. In addition reference cases, simulations where thermophoresis have not been taken into account, have been performed both for isothermal and non-isothermal flow for $\mathrm{Re} = 20$ and $\mathrm{Re} = 380$.

The ratio between the front side particle impaction efficiency in the non-isothermal reference case and the isothermal reference case for the smallest Stokes numbers considered was expected to be proportional to the ratio of the free stream temperature and the cylinder temperature, according to analytical considerations. The simulations for $\mathrm{Re} = 20$ was in good agreement with this relation, but for $\mathrm{Re} = 380$ the front side particle impaction efficiency for the smallest particles was lower in the non-isothermal reference case compared to the isothermal reference case. This is believed to have been caused by inaccuracies in the numerical method for the non-isothermal simulation at $\mathrm{Re} = 380$.

Thermophoresis was not found to affect the particle impaction for the largest Stokes numbers. For intermediate and small Stokes numbers the effect of thermophoresis depended on Λ. The particle impaction efficiency was significantly higher, both for the front side and the back side, in the thermophoretic simulations compared to the non-isothermal reference case for particles with $\Lambda = 1$ and $\Lambda = 100$. The particle impaction efficiency for particles with $\Lambda = 1000$ was lower, both for the front side and the back side, in the thermophoretic case compared to the non-isothermal reference case.

Sammendrag

Effekten av termoforese på partikelavsetningen på en kald sylinder i ikke-isoterm laminær gass-strømning har blitt studert ved hjelp av Direkte Numeriske Simuleringer (DNS). Simuleringer hvor termoforese var inkludert for forskjellige Stokes tall og forskjellige forhold mellom partiklenes varmeledningsevne og gassens varmledningsevne, Λ, blitt utført for Reynolds tall $\mathrm{Re} = 380$. I tillegg har referansesimuleringer, simuleringer der termoforese ikke var inkludert, har blitt utført både for ikke-isoterm og isoterm strømning for $\mathrm{Re} = 20$ og $\mathrm{Re} = 380$.

Forholdet mellom antallet partikelkollisjoner på forsiden av sylinderen for den isoterme og den ikke-isoterme referansesimuleringen for små Stokes tall var forventet å være proporsjonal med forholdet mellom temperaturen på den innkommende gassen og temperaturen på sylinderen, i henhold til analytiske vurderinger. Denne relasjonen stemte godt overens med simuleringene for $\mathrm{Re} = 20$, men for $\mathrm{Re} = 380$ var antallet partikelkollisjoner på forsiden av sylinderen lavere i det ikke-isoterme tilfellet i forhold til det isoterm tilfelle for små Stokes tall. Det var trolig grunnet unøyaktigheter i den numeriske metoden for ikke-isoterm strømning ved $\mathrm{Re} = 380$.

Termoforese påvirket ikke antallet partikelkollisjoner på sylinderen for de største Stokes tallene. For middels store og små Stokes tall var antall partikelkollisjoner på sylinderen avhengig av Λ. Antall partikelkollisjoner, både på forsiden og baksiden, var betydelig høyere for simuleringene med termoforese for partikler med $\Lambda = 1$ og $\Lambda = 100$, i forhold til den ikke-isoterme referansesimuleringen. Antallet partikkelkollisjoner, både på forsiden og baksiden, på sylinderen var lavere for simuleringen med termoforese for partikkler med $\Lambda = 1000$, i forhold til den ikke-isoterme referansesimuleringen.

Preface

This thesis has been done as a part of the subject TFY4200, which is the finalization of my Master's Degree in Applied Physics and Mathematics. The work has been done in collaboration with SINTEF Energy Research and the Department of Physics at NTNU. The thesis is a continuation of the work done in my specialization project during the autumn of 2011. All results presented in this thesis are from simulations done this spring.

Acknowledgements

First of all I would like to thank Nils Erland Haugen for providing an interesting assignment and for being very helpful when I have been facing challenges. I am also grateful for the computing time I have been granted at the cluster at SINTEF Energy Research. My supervisor at the Department of Physics Jon Andreas Støvneng have always been very helpful. I am thankful to Rune Øistein Aas for discovering errors and for giving valuable advice.

Trondheim, June 7. 2012 Henrik Fahre Lutro.

Contents

Chapter 1

Introduction

Particle deposition is interesting for a wide range of applications, and thermophoresis is a phenomenon which might have an impact on particle deposition in gases with temperature gradients.

1.1 Motivation

Although particles embedded flow surrounds us on a daily basis, it is very complicated to describe the exact motion. The motion of the particles will depend on the flow field of the gas and effects such as Brownian motion, thermophoresis, electrophoresis and turbophoresis.

Particle deposition is of interest for several industrial applications, air filters rely on particles depositing on the surface of the filter, so do different coating techniques for chemicals. For other applications such as industrial boilers, furnaces and heat exchangers it is desirable to minimize the particle deposition.

The motivation for this project is to increase the efficiency of bio energy plants. Biomass was the dominant energy source up to the 19th century, and is still one of the most important sources of energy. But it is mainly used as a heat source. The use of biomass and municipal solid waste for electricity production have been limited due to the poor efficiency of the power plants. A bio energy plant functions by combusting the biomass and let the flue gas transfer the heat to tubes containing a fluid, for example water/steam. To achieve high efficiency super heated steam is needed, which means temperatures in the order of 500 °C, these temperatures are achieved by heating the water/steam several times. This is the same process as in coal plants, but when bio-waste is combusted residue particles transported with the flue gas are partly melted and will stick to the tubes, see figure 1.1. Combustion of bio-waste leads to a much larger amount of partly melted residue particles

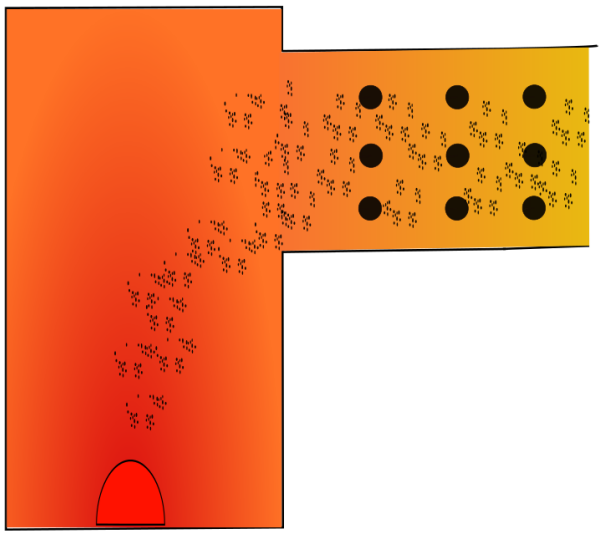

Figure 1.1: Combustion of biomass in a bio energy plant leads to particle deposition on the tubes containing water/steam

than in coal plants. Particles impacting on the tubes will lead to an insulating layer on the tubes causing decreased efficiency of the heat transfer. If the residue particles consist of salt they may cause corrosion leading to damage on the tubes, and if the particle deposition is substantial it can lead to obstruction of the gas flow past the tubes.

In order to optimize the efficiency of bio energy plants the particle impaction on the tubes needs to be minimized, in order to achieve this the mechanisms behind particle deposition on a cylinder needs to be understood. The aim of this study is to improve the existing model by taking into account the effects of temperature gradients in the gas.

1.2 Important concepts

In this subsection some general concepts will be discussed and previous work on various relevant topics will be presented.

1.2.1 Particle deposition

For a particle to deposit on a surface it is required that the particle hits the surface and that it sticks to it. These requirements are described by the particle impaction efficiency and the particle adsorption coefficient, respectively. In this work the focus will be on the particle impaction efficiency. Which is defined as the ratio between the number of particles hitting the surface, N_{surface} and the number of particles initially directed towards the cylinder, N_0,

$$\eta = \frac{N_{\text{surface}}}{N_0}. \tag{1.1}$$

As the fluid approaches a cylinder the flow will be deflected around the surface, a particle immersed in the fluid will therefore experience a force directed away from the cylinder due to the drag from the fluid. The particles will be affected by the drag in varying degree depending on the size of the particles, the smallest particles will follow the flow to a much greater extent than the largest particles. The particle impaction efficiency will therefore depend both on the incoming flow and the particles immersed in the flow. The case was first treated theoretically with potential flow theory by Israel and Rosner (1982) [1], since it for potential flow theory exists analytical solutions of the flow field around a cylinder. Potential theory does not describe the viscous boundary layer near the cylinder where the particle impaction takes place, is therefore insufficient for small particles. Haugen and Kragset (2010) [2] looked at the particle deposition on a cylinder assuming isothermal and laminar flow with Direct Numerical Simulation (DNS), which resolves the boundary layer, for different values of Reynolds and Stokes numbers. In this context laminar refers to the incoming laminar flow.

Since there will be a difference between the temperature of the incoming gas and the temperature of the cylinder in a heat exchanger it is unrealistic to assume isothermal flow. To obtain a realistic model of the situation the effect of temperature gradients must be determined. Temperature gradients in the gas will have two effects; the flow field will be different and the thermophoretic force will act on the particles.

1.2.2 Thermophoresis

The thermophoretic force is the force on particles submerged in a gas or liquid with a temperature gradient. The direction of the force is opposite to the temperature gradient. The effect was first observed in 1870 by Tyndall [3], when he observed that a particle free zone around a heated surface appeared in dusty air. In 1884 Aitken [4] proved that the microscopic explanation to the effect was due to the heavier bombardment of the particle from the gas molecules on the hot side compared to the cold side. The phenomenon where particles are influenced by the thermophoretic force is called thermophoresis. There are many applications of thermophoresis and cases where this effect play an important part; e.g. filters, particle deposition on boilers and different measurement techniques for aerosols during combustion.

There has been done much theoretical and experimental work on the subject since the discovery of thermophoresis, but due to the complexity of the governing equations there is still no complete analytical solution to the problem. The thermophoretic force is caused by differences in the velocity distribution of the gas particles, therefore the velocity distribution of the gas molecules must be found in order to calculate the net momentum transfer. The governing equation is the Boltzmann equation for a gas with temperature gradient. At present a general analytical solution of the equation does not exist, however for certain approximations analytical solutions exist.

In many applications a fluid can be considered a continuum, i.e. only the overall motion of the particles is considered and not the individual motion of every particle, then the Navier-Stokes equations for the fluid flow and Fourier's equation for the heat flow can be used. However in gases where the size of an object submerged in the gas is small compared to the the mean free path of the gas, λ, then the gas can no longer be considered a continuum. The gas is then referred to as rarefied and the general equation for a fluid, the Boltzmann equation, must be used. Which is the case for microscopic particles submerged in a gas or when the gas has very low density (very high mean free path). The ratio between the mean free path of the gas and the characteristic length, a, of an object is called the Knudsen number

$$\mathrm{Kn} = \frac{\lambda}{a}, \tag{1.2}$$

for a spherical particle $a = r_\mathrm{p}$, where r_p is the particle radius. The mean free path of a gas is the average distance a gas molecule travels between collisions with other gas molecules. In Shen [5] the following relation is given

$$\mu = \frac{1}{2}\rho\bar{c}\lambda, \tag{1.3}$$

where μ is the dynamic viscosity and ρ is the mass density of the gas. The average molecular speed, $\bar{c}$, of a gas molecule with mass M for an ideal gas

is

$$\bar{c} = \sqrt{\frac{8k_\mathrm{b}T}{\pi M}}, \tag{1.4}$$

where k_b is the Boltzmann constant. By rearranging the following expression for λ is obtained

$$\lambda = \nu\sqrt{\frac{\pi M}{2k_\mathrm{b}T}}. \tag{1.5}$$

Some definitions of the mean free path differ from this definition by a constant factor

$$\hat{\lambda} = \frac{2}{\sqrt{\pi}}, \tag{1.6}$$

as in Zheng [6]. A gas is considered rarefied if $\mathrm{Kn} \gtrsim 0.01$, and can be divided into different regimes defined by the Knudsen number, as in Shen [5];

Near continuum region:	$\mathrm{Kn} \lesssim 0.1$
Transition region:	$0.1 \lesssim \mathrm{Kn} \lesssim 10$
Free molecule region:	$\mathrm{Kn} \gtrsim 10$

The Navier-Stokes-Fourier equations of classical fluid mechanics can still be used in the near continuum region, but the boundary conditions at the surface of the object must be changed. The mean free path of air under atmospheric conditions is about 67 nm, which means that rarefied gas dynamics must be used if the characteristic length of an object is $a \sim 1$ μm.

For most traditional engineering applications the continuum hypothesis is therefore valid and classical fluid mechanics can be used, but there are several applications where rarefied gas dynamics must be taken into account. Particle deposition as is the topic of this study is one case, other examples are high altitude or space flight (where the mean free path is very high) and nano machines. It must be noted that although thermophoresis is not described by classical fluid mechanics it does not vanish when the continuum limit of the rarefied gas is taken. For the two extreme cases $\mathrm{Kn} \to 0$ (the continuum limit) and $\mathrm{Kn} \to \infty$ (the free molecule limit) analytical solutions have been derived for spherical particles and mono atomic gases. In the transition region only numerical solutions exists.

In the continuum limit the Boltzmann equation reduces to the Navier-Stokes equation. By using continuum fluid mechanics with the correct slip flow boundary conditions the problem for $\mathrm{Kn} << 1$ can be solved. This method was first used by Epstein in 1929 [7] and later expanded by using the complete slip conditions by Brock in 1962 [8]. This gives a non zero thermophoretic force which is not described by classical fluid mechanics the reason behind this is that the boundary conditions given by classical fluid mechanics are not correct for gases with temperature gradients, this will

discussed in subsection 2.2.1. In the free molecule regime the velocity distribution of the gas molecules is considered unaffected by the presence of a particle. The velocity distribution can then be found, this was first done by Waldmann in 1959 [8].

As there is no general solution for the transition regime and expansion of the two limits into the transition region has proven unsuccessfull the only alternative is to solve the Boltzmann equation numerically, however solving it in its full form can be difficult therefore simplifications are usually done to the Boltzmann equation before it is solved numerically. Before accurate numerical results existed an interpolation formula by Talbot et al [9] was widely used and is still used today for practical applications. Most of the work done on thermophoresis, both theoretical and experimental, is limited to spheres. The few results on non-spherical particles is restricted to the free molecule and near continuum regime, and they indicate that the shape and orientation of the particles is important. The theory also assumes mono atomic gas, the usual method is to use the translational part of the thermal conductivity instead of the full thermal conductivity when considering polyatomic gases.

Several numerical results (see e.g. Young [10]) have shown a thermophoretic force in the direction of the temperature gradient when the thermal conductivity of the particle is high compared to the gas, since it is opposite of the usual direction it is called reversed or negative thermophoresis. However since this never has been verified experimentally and since negative thermophoresis is a weak effect compared to positive thermophoresis it might be a result of the numerical method.

Obtaining accurate measurements of the thermophoretic force is difficult due to the small size of the particles. Data for spherical particles agrees well with the theoretical results see e.g. Young [10] or Zheng [6] for various comparisons. The Waldmann limit has to a great extent been verified, but the Epstein limit has not been verified. The accuracy of the current models is limited by the assumptions of mono atomic gas and spherical particles, when most gases are polyatomic and most particles are non-spherical as well as the simplifications done when solving the Boltzmann equation.

Thermophoresis has been included in many studies of particle deposition. Shen [11] found theoretical expressions for the thermophoretic deposition on a cold cylinder in laminar incoming flow by using numerical solutions of the boundary layer and by using an expression for the thermophoretic velocity based on the interpolation formula by Talbot [9]. Chiou and Cleaver [12] studied the particle deposition on a heated cylinder and found that this reduced the particle deposition by two orders of magnitude for the particles studied. An experimental study showed that the absolute values of the deposition were greater than the theoretical result, but the the magnitude of

the difference between the isothermal and non-isothermal deposition from the theoretical study was in good agreement with the experimental. There have also been several studies on thermophoretic deposition on channel walls see e.g. Chiou, Chiu and Chen [13]

1.3 Aim and overview of the thesis

Previous work on thermophoretic deposition on a cylinder, does not employ DNS, and previous work on deposition on a cylinder with DNS does not include thermophoresis. The aim of this study is to determine the effect of thermophoresis on the particle deposition on a cooled cylinder by using DNS. The determining equations for the fluid and particle motion are presented in chapter 2. In chapter 3 details of the numerical method used in the simulations will be presented. Since thermophoresis is a phenomenon which arises in non-isothermal flow, the non-isothermal fluid implementation needs to be verified. This has been done by comparing non-isothermal reference cases to corresponding isothermal reference cases. Where non-isothermal reference case refers to a case where temperature gradients have been accounted for in the fluid implementation, but thermophoresis has not been taken into account in the description of the particle motion. Results for these cases are presented and discussed in chapter 4. In chapter 5 results from thermophoretic simulations with $\mathrm{Re} = 380$ is compared to the results from the corresponding non-isothermal reference case and the effect of thermophoresis is discussed. Then conclusions based on the discussion of the reference cases and the thermophoretic cases are made.

Chapter 2

Equations

There are two ways of looking at motion of particles; the Lagrangian and the Eulerian formalism. In the Lagrangian formalism one tracks every single particle and its momentum, energy and position, while in the Eulerian formalism one tracks momentum and energy at a specific location. In this study the Lagrangian formalism has been used for the particle motion, while the Eulerian formalism has been used for the fluid motion. The Eulerian formalism is valid as long as the fluid can be considered a continuum, close to small particles this assumption does not hold. Therefore the thermophoretic force and the Stokes-Cunningham factor are introduced. Only one-way fluid-particle interaction is assumed, i.e. the fluid affects the particles, nut the particles do not influence the fluid.

2.1 Fluid equations

Many different non-dimensional parameters can be used to describe fluid flows, depending on the nature of the flow. Some of these parameters are defined by temperature dependent quantities. In order to compare the non-isothermal case to the isothermal case the values of these quantities will be evaluated at the free stream temperature.

The determining parameter for a fluid flow is the Reynolds number, Re, which is a measure of the ratio between inertial and viscous forces. The Reynolds number is defined as

$$\mathrm{Re} = \frac{uL}{\nu}, \tag{2.1}$$

where u is a characteristic velocity, $\nu = \frac{\mu}{\rho}$ is the kinematic viscosity, μ is the dynamic viscosity, ρ is the fluid mass density and L is a characteristic length. In the case of flow around a cylinder; $u = u_0$ and $L = D$, where u_0 is the

velocity of the incoming flow and D is the diameter of the cylinder.

There are two modes of heat transfer in a fluid; convection and conduction. Convection is heat transferred by the flow of the fluid, while conduction is carried on through molecular interactions. An important parameter for heat convection is the Prandtl number. The Prandtl number, Pr, is defined as the ratio of the dissipation and the conduction

$$\mathrm{Pr} = \frac{\nu}{\chi} = \frac{\mu}{\rho}\frac{\rho c_\mathrm{p}}{k} = \frac{c_\mathrm{p}\mu}{k}, \tag{2.2}$$

where $\chi = \frac{k}{\rho c_\mathrm{p}}$ is the thermal diffusivity, k is the heat conductivity and c_p is the specific heat capacity at constant pressure.

When an incoming flow approaches a cylinder the streamlines will be deflected around the cylinder. If the Reynolds number is above a certain threshold an unsteady flow develops where Von Kármán eddies are found behind the cylinder, as seen behind the pillars of a bridge across a river. Williamson [14] found this threshold to be $\mathrm{Re}_{\mathrm{Kármán}} = 49$. The non-dimensional measure of the frequency of the eddies, f, is the Strouhal number, for a cylinder it is defined as

$$\mathrm{Str} = \frac{f}{1/\tau_\mathrm{f}}, \tag{2.3}$$

where

$$\tau_\mathrm{f} = D/u_0 \tag{2.4}$$

is the typical fluid relaxation time.

In order to accurately resolve the boundary layer Direct Numerical Simulation (DNS) is used, as the name suggest DNS involves solving the determining fluid equations directly without any modeling. Even for relatively low Reynolds numbers DNS is very computationally demanding. The method used in the simulations will be discussed in more detail in chapter 3.

2.1.1 Classical fluid mechanics

Classical fluid mechanics will be used for the fluid implementation, classical fluid mechanics assumes that the fluid is a continuum. The more general description will be presented in subsection 2.1.2. Two central assumptions in classical fluid mechanics are the boundary conditions at a solid wall. The no slip condition states that the fluid at a solid boundary will have a velocity identical to the solid. The no temperature jump condition states, in a similar way, that the temperature of the fluid at the surface must be equal to the temperature of the surface.

For a fluid the total mass of the system must be conserved, the change of

mass in a volume element Ω is equal to the flux through the surface $\partial\Omega$ of Ω,

$$\frac{\partial}{\partial t}\int_{\Omega}\rho \mathrm{d}V = -\int_{\partial\Omega}\rho \boldsymbol{u}\cdot\boldsymbol{n}\mathrm{d}A, \tag{2.5}$$

where $\mathrm{d}V$ is a infinitesimal volume element of Ω, $\mathrm{d}A$ a infinitesimal surface element of $\partial\Omega$, $\boldsymbol{n}$ the normal vector of $\mathrm{d}A$ and $\boldsymbol{u}$ the fluid velocity. The time derivative can be taken inside the integral since the volume element can be assumed constant. The surface integral can be evaluated as a volume integral by using the divergence theorem,

$$\int_{\Omega}\frac{\partial\rho}{\partial t}\mathrm{d}V = -\int_{\Omega}\nabla\cdot(\rho\boldsymbol{u})\mathrm{d}V = -\int_{\Omega}(\rho\nabla\cdot\boldsymbol{u}+(\boldsymbol{u}\cdot\nabla)\rho)\mathrm{d}V. \tag{2.6}$$

By assuming zero gradients within the volume element the integrand on the left hand side must equal the integrand on the right hand side,

$$\frac{\partial\rho}{\partial t} = -(\rho\nabla\cdot\boldsymbol{u}+(\boldsymbol{u}\cdot\nabla)\rho). \tag{2.7}$$

Using the advective derivative $\frac{\mathrm{D}}{\mathrm{Dt}} = \frac{\partial}{\partial t}+\boldsymbol{u}\cdot\nabla$ and rearranging yields the continuity equation,

$$\frac{\mathrm{D}\rho}{\mathrm{D}t} = -\rho\nabla\cdot\boldsymbol{u}. \tag{2.8}$$

The equivalent to Newtons second law in fluid mechanics is the Navier-Stokes equation, obtained from conservation of momentum. The change in momentum of a fluid volume element is equal to the force exerted on the control volume by external forces and the momentum flux, in this case no other forces than the pressure and the viscous forces are considered,

$$\frac{\partial}{\partial t}\int_{\Omega}\rho\boldsymbol{u}\mathrm{d}V + \int_{\partial\Omega}\rho\boldsymbol{u}\boldsymbol{u}\cdot\mathbf{n}\mathrm{d}A = -\int_{\partial\Omega}\mathbf{P}\cdot\mathbf{n}\mathrm{d}A + \int_{\partial\Omega}2\mu\mathbf{S}\cdot\mathbf{n}\mathrm{d}A, \tag{2.9}$$

where $\mathbf{P} = P\cdot\mathbf{I}$ is the pressure tensor, P is the pressure, $\mathbf{I}$ is the unit tensor and $\mathbf{S}$ is the traceless rate of stress tensor. By assuming Newtonian fluid

$$\mathbf{S} = \frac{1}{2}(\nabla\boldsymbol{u}+(\nabla\boldsymbol{u})^{\mathrm{T}}) - \frac{1}{3}\mathbf{I}\nabla\cdot\boldsymbol{u}, \tag{2.10}$$

and using the divergence theorem equation (2.9) can be written as

$$\frac{\partial\rho\boldsymbol{u}}{\partial t} + \nabla\cdot(\rho\boldsymbol{u}\boldsymbol{u}) = -\nabla P + \nabla\cdot(2\mu\mathbf{S}). \tag{2.11}$$

The left hand side of the equation can be simplified

$$\begin{aligned}\frac{\partial\rho\boldsymbol{u}}{\partial t} + \nabla\cdot(\rho\boldsymbol{u}\boldsymbol{u}) &= \rho\frac{\partial\boldsymbol{u}}{\partial t} + \boldsymbol{u}\frac{\partial\rho}{\partial t} + \rho\boldsymbol{u}\cdot\nabla\boldsymbol{u} + \rho\boldsymbol{u}\nabla\cdot\boldsymbol{u} + \boldsymbol{u}\boldsymbol{u}\cdot\nabla\rho \\ &= \rho\frac{\mathrm{D}\boldsymbol{u}}{\mathrm{D}t} + \boldsymbol{u}\frac{\mathrm{D}\rho}{\mathrm{D}t} + \rho\boldsymbol{u}\nabla\cdot\boldsymbol{u}.\end{aligned} \tag{2.12}$$

By using the continuity equation (2.8) the left hand side of equation (2.11) reduces to $\rho\frac{\mathrm{D}\boldsymbol{u}}{\mathrm{D}t}$ and the compressible Navier-Stokes equation without an external force field is given by

$$\rho\frac{\mathrm{D}\boldsymbol{u}}{\mathrm{D}t} = -\nabla P + \nabla\cdot(2\mu\mathbf{S}). \tag{2.13}$$

Conservation of energy gives the following expression for temperature, as implemented in The Pencil Code [15],

$$\frac{\partial T}{\partial t} = -\boldsymbol{u}\cdot\nabla T + \frac{k}{\rho c_{\mathrm{v}}}\nabla^2 T + 2\frac{\nu}{c_{\mathrm{v}}}\mathbf{S}^2 - (\gamma-1)T\nabla\cdot\boldsymbol{u}, \tag{2.14}$$

where $\gamma = \frac{c_{\mathrm{p}}}{c_{\mathrm{v}}}$, c_{p} and c_{v} are the specific heat capacities for constant pressure and volume respectively. In addition to these equations an equation of state for the gas is needed, if ideal gas is assumed the following expression is given

$$P = \rho R T, \tag{2.15}$$

where $R = c_{\mathrm{p}} - c_{\mathrm{v}}$, is the specific gas constant.

In general both viscosity and thermal conductivity are temperature dependent, the exact dependency on temperature is determined by the properties of the fluid. In order to incorporate the effects of temperature a simple model based on mono atomic gas where the gas molecules are considered to be rigid spheres has been used. According to Chapman and Cowling [16] this gives the following temperature dependence

$$\frac{\mu}{\mu_0} = \sqrt{\frac{T}{T_0}}, \tag{2.16}$$

$$\frac{k}{k_0} = \sqrt{\frac{T}{T_0}}, \tag{2.17}$$

where μ_0 and k_0 are the dynamical viscosity and the thermal conductivity at a reference temperature T_0.

2.1.2 The Boltzmann equation

The Boltzmann equation or the Boltzmann transport equation describes the statistical distribution of a molecule in a fluid, the Boltzmann equation is the general equation for a fluid. The solution of the Boltzmann equation is the probability density f in phase-space, defined such that the probability of finding a molecule with mass M and momentum between $\boldsymbol{p}$ and $\boldsymbol{p}$+d$\boldsymbol{p}$ and position between $\boldsymbol{x}$ and $\boldsymbol{x}$+d$\boldsymbol{x}$ at time t is given by $f(\boldsymbol{x},\boldsymbol{p},t)\mathrm{d}\boldsymbol{x}\mathrm{d}\boldsymbol{p}$. For a gas

without collisions the following relation for the distribution $f(\boldsymbol{x}, \boldsymbol{p}, t)$ must hold

$$f(\boldsymbol{x} + \frac{\boldsymbol{p}}{M}\mathrm{d}t, \boldsymbol{p} + \boldsymbol{F}\mathrm{d}t, t + \mathrm{d}t)\mathrm{d}\boldsymbol{x}\mathrm{d}\boldsymbol{p} = f(\boldsymbol{x}, \boldsymbol{p}, t)\mathrm{d}\boldsymbol{x}\mathrm{d}\boldsymbol{p}. \tag{2.18}$$

The equation then states that a molecule with position $\boldsymbol{x}$ and momentum $\boldsymbol{p}$ at time t will under influence of a force, $\boldsymbol{F}$, be at position ,$\boldsymbol{x}+\boldsymbol{v}\mathrm{d}t = \boldsymbol{x}+\frac{\boldsymbol{p}}{M}\mathrm{d}t$, and have momentum $\boldsymbol{p}+\boldsymbol{F}\mathrm{d}t$ at time ,$t+\mathrm{d}t$, where $\mathrm{d}t$ is a small time interval. However when collisions occur the density of particles in the phase-space volume $\mathrm{d}\boldsymbol{x}\mathrm{d}\boldsymbol{p}$ changes,

$$\begin{aligned} &f(\boldsymbol{x} + \frac{\boldsymbol{p}}{M}\mathrm{d}t, \boldsymbol{p} + \boldsymbol{F}\mathrm{d}t, t + \mathrm{d}t)\mathrm{d}\boldsymbol{x}\mathrm{d}\boldsymbol{p} \\ &- f(\boldsymbol{x}, \boldsymbol{p}, t)\mathrm{d}\boldsymbol{x}\mathrm{d}\boldsymbol{p} = \left.\frac{\partial f(\boldsymbol{x}, \boldsymbol{p}, t)}{\partial t}\right|_{\mathrm{coll}} \mathrm{d}\boldsymbol{x}\mathrm{d}\boldsymbol{p}\mathrm{d}t. \end{aligned} \tag{2.19}$$

The collision term represents the change in position and momentum of the particle caused by collisions with other particles. Dividing with $\mathrm{d}\boldsymbol{x}\mathrm{d}\boldsymbol{p}\mathrm{d}t$ on both sides and taking the limit $\mathrm{d}\boldsymbol{x} \to 0, \mathrm{d}\boldsymbol{p} \to 0$ and $\mathrm{d}t \to 0$ yields the Boltzmann equation,

$$\frac{\partial f}{\partial t} + \frac{\boldsymbol{p}}{M}\frac{\partial f}{\partial \boldsymbol{x}} + \boldsymbol{F}\frac{\partial f}{\partial \boldsymbol{p}} = \left.\frac{\partial f}{\partial t}\right|_{\mathrm{coll}}. \tag{2.20}$$

The Boltzmann equation is highly nonlinear and especially the collision term makes it very difficult to solve. In equilibrium with no external forces and neglecting the collision term the solution of equation (2.20) can be shown to be the Maxwell distribution,

$$f = \left(\frac{1}{2\pi M k_{\mathrm{b}} T}\right)^{3/2} e^{-\frac{\boldsymbol{p}^2}{2Mk_{\mathrm{b}}T}}, \tag{2.21}$$

where k_{b} is the Boltzmann constant. Alternatively the Maxwell distribution can be given in terms of the molecule velocity, $\boldsymbol{c}$, instead of momentum

$$\begin{aligned} f &= \left(\frac{M}{2\pi k_{\mathrm{b}} T}\right)^{3/2} e^{-\frac{M\boldsymbol{c}^2}{2k_{\mathrm{b}}T}}, \\ &= \left(\frac{\beta}{\sqrt{\pi}}\right)^{3} e^{-\beta^2 c^2}, \end{aligned} \tag{2.22}$$

where $\beta = \sqrt{\frac{M}{2k_{\mathrm{b}}T}}$. If the probability density function is known quantities like density, momentum and pressure can be calculated. Then equations for conservation of mass, momentum and energy can be derived. Shen [5] shows that the zeroth order with respect to Knudsen number of the momentum equation is the Euler equations and the first order is the Navier-Stokes equation.

2.2 Particle equations

The motion of a particle is determined by Newtons second law $\boldsymbol{F} = m_{\mathrm{p}}\boldsymbol{a}$. The acceleration, $\boldsymbol{a}$, of a particle with mass m_{p} is proportional to the force, $\boldsymbol{F}$, on the particle. The forces on the particle in a situation like this can be the drag force from the fluid, gravity, electric forces, particle-particle interaction, thermophoretic force and Brownian forces. Gravity is neglected considering the small size of the particles, particle-particle interaction is not considered since there is relatively low particle concentration in the flue gases in typical industrial boilers. Thermophoresis is a more general phenomenon than electrophoresis, since temperature gradients obviously will be found in an industrial boiler, while the particles are not necessarily charged or placed in an electric field. Unlike the thermophoretic force Brownian forces are not necessarily directed towards cylinder and will therefore probably be a weaker effect. The forces on the particles considered in this study will therefore be limited to the drag force and the thermophoretic force.

2.2.1 The thermophoretic force

It is not within the scope of this study to go into details of the derivation of the expression for the thermophoretic force, but some results from the near continuum region will be presented to give an understanding of the phenomenon. The thermophoretic force is due to the interaction between the gas molecules and the particles, this is usually modeled by assuming that a fraction α of the incident particles is reflected diffusively and the rest specularly. Specular comes from Latin and means mirror, i.e. the molecules are reflected as light rays on a mirror, the momentum tangential to the surface is conserved and the momentum normal to the surface reversed. In the diffusive model the incoming molecules colliding with the particle are assumed to be in equilibrium with the particle surface and leave the surface with a Maxwellian velocity distribution given by the temperature at the particle surface. Different values for the momentum and energy transfer coefficients α_{m} and α_{e} can be used. Then the momentum and energy fluxes can be defined as

$$\begin{aligned} \dot{p}_{\mathrm{ref}} &= -(1-\alpha_{\mathrm{p}})\dot{p}_{\mathrm{inc}} + \alpha_{\mathrm{p}}\dot{p}_{\mathrm{eqm}}, \\ \dot{E}_{\mathrm{ref}} &= -(1-\alpha_{\mathrm{e}})\dot{E}_{\mathrm{inc}} + \alpha_{\mathrm{e}}\dot{E}_{\mathrm{eqm}}, \end{aligned} \tag{2.23}$$

where $\dot{p}$ and $\dot{E}$ denotes the tangential momentum and kinetic energy fluxes. The subscripts 'inc', 'ref' and 'eqm' denotes the incoming molecules, the reflected molecules and the molecules with velocity distribution given by the

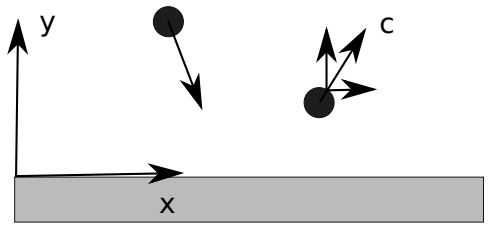

Figure 2.1: Incoming molecule and reflected molecule at a flat wall

Maxwellian distribution at the surface. The values of α_e and α_p will lie somewhere between 0 and 1, but the exact value is difficult to determine since it will depend on the material of the particle, the gas molecules and the state of the surface. Most estimates of the values are close to 1, and therefore a value of 1 will be used as in Young [10], which means diffusive scattering only.

In order to derive the boundary conditions in the near continuum region the first order Chapman-Enskog approximation can be used, as in Shen [5]. Consider the gas molecules close to a flat wall, one part of the molecules will approach the wall, while the other part has been reflected off the wall. The geometry of the problem is shown in figure 2.1. By taking the average velocity of the gas molecules the velocity of the gas is obtained, where u is the gas velocity in the x-direction and u_s is the gas velocity in x-direction at the surface. The flux of x-momentum of one molecule with mass M is defined as the change in momentum par unit area

$$\dot{p} = \frac{M}{V} c_x c_y. \tag{2.24}$$

By using the first order Chapman-Enskog approximation

$$f_{\mathrm{s}} = f_0 \left[1 - \frac{4k\beta^2}{5nk_{\mathrm{b}}} \left(\beta^2 c'^2 - \frac{5}{2}\right) c'_{\mathrm{x}} \frac{1}{T}\frac{\partial T}{\partial x} - \frac{4\mu\beta^4}{\rho} c'_{\mathrm{x}} c'_{\mathrm{y}} \frac{\partial u_0}{\partial y}\right], \tag{2.25}$$

where f_0 is the Maxwell distribution, the momentum fluxes for the incoming and the reflected molecules can be calculated

$$\begin{aligned} \dot{p} &= \int_{-\infty}^{\infty}\int_{-\infty}^{\infty}\int_{-\infty}^{\infty} Mn(c'_{\mathrm{x}} + u_{\mathrm{s}}) c'_{\mathrm{y}} f_{\mathrm{s}} d\boldsymbol{c'}, \\ \dot{p}_{\mathrm{inc}} &= \int_{-\infty}^{\infty}\int_{-\infty}^{0}\int_{-\infty}^{\infty} Mn(c'_{\mathrm{x}} + u_{\mathrm{s}}) c'_{\mathrm{y}} f_{\mathrm{s}} d\boldsymbol{c'}, \\ \dot{p}_{\mathrm{eqm}} &= \int_{-\infty}^{\infty}\int_{0}^{\infty}\int_{-\infty}^{\infty} Mn(c'_{\mathrm{x}} + u_{\mathrm{s}}) c'_{\mathrm{y}} f_0 d\boldsymbol{c'}, \end{aligned} \tag{2.26}$$

where n is the number of molecules per volume. Which means that

$$\dot{p}_{\mathrm{eqm}} = 0. \tag{2.27}$$

The total momentum is the sum of the momentum of the incoming and reflected molecules

$$\dot{p} = \dot{p}_{\mathrm{inc}} - (1 - \alpha_{\mathrm{p}})\dot{p}_{\mathrm{spec}} + \alpha_{\mathrm{p}}\dot{p}_{\mathrm{eqm}} = \alpha_{\mathrm{p}}\dot{p}_{\mathrm{inc}}. \tag{2.28}$$

Calculating $\dot{p}_{\mathrm{inc}}$ gives

$$\begin{aligned} \dot{p}_{\mathrm{inc}} = &\int_{-\infty}^{\infty}\int_{-\infty}^{0}\int_{-\infty}^{\infty} c'_{\mathrm{y}}\left(u_{\mathrm{s}} + c'_{\mathrm{x}}\right) Mn \left(\frac{\beta^3}{\pi^{3/2}}\right) e^{-\beta^2 c'^2} \times \\ &\left[1 - \frac{4k\beta^2}{5nk_{\mathrm{b}}} \left(\beta^2 c'^2 - \frac{5}{2}\right) c'_{\mathrm{x}} \frac{1}{T}\frac{\partial T}{\partial x} - \frac{4\mu\beta^4}{\rho} c'_{\mathrm{x}} c'_{\mathrm{y}} \frac{\partial u_0}{\partial y}\right] \mathrm{d}\boldsymbol{c'}, \end{aligned} \tag{2.29}$$

rearranging one obtains

$$\begin{aligned} \dot{p}_{\mathrm{inc}} = &\int_{-\infty}^{\infty}\int_{-\infty}^{0}\int_{-\infty}^{\infty} Mn \left(\frac{\beta^3}{\pi^{3/2}}\right) e^{-\beta^2 c'^2} \times \\ &\left[c'_{\mathrm{y}} u_{\mathrm{s}} + c'_{\mathrm{x}} c'_{\mathrm{y}} - \frac{4k\beta^2}{5nk_{\mathrm{b}}} \left(\beta^2 c'^2 - \frac{5}{2}\right) \frac{1}{T}\frac{\partial T}{\partial x}(c'_{\mathrm{y}} c'^2_{\mathrm{x}} + c'_{\mathrm{y}} c'_{\mathrm{x}} u_{\mathrm{s}})\right. \\ &\left. - \frac{4\mu\beta^4}{\rho}\frac{\partial u_0}{\partial y}(c'^2_{\mathrm{x}} c'^2_{\mathrm{y}} + c'_{\mathrm{x}} u_{\mathrm{s}} c'^2_{\mathrm{y}})\right] \mathrm{d}\boldsymbol{c'}, \end{aligned} \tag{2.30}$$

the terms with an odd exponent of c'_{x} will give zeros. Integrating the remaining terms gives,

$$\dot{p}_{\mathrm{inc}} = -\frac{1}{2} Mn \frac{u_{\mathrm{s}}}{\beta\sqrt{\pi}} + \frac{1}{10} Mn \frac{k}{\beta n k_{\mathrm{b}}\sqrt{\pi}} \frac{1}{T}\frac{\partial T}{\partial x} - \frac{1}{2} Mn \frac{\mu}{\rho}\frac{\partial u_0}{\partial y}. \tag{2.31}$$

For $\dot{p}$ the terms with an odd exponent of c'_{y} will give zeros as well and

$$\dot{p} = -Mn\frac{\mu}{\rho}\frac{\partial u_0}{\partial y}. \tag{2.32}$$

Using equation (2.28), (2.31) and (2.32) yields

$$2\sqrt{\pi}\frac{\mu\beta}{\rho}\frac{\partial u_0}{\partial y} = \alpha_{\mathrm{p}}\left(u_{\mathrm{s}} - \frac{1}{5}\frac{k}{nk_{\mathrm{b}}}\frac{1}{T}\frac{\partial T}{\partial x} + \sqrt{\pi}\frac{\mu\beta}{\rho}\frac{\partial u_0}{\partial y}\right), \tag{2.33}$$

and isolating for u_{s},

$$u_{\mathrm{s}} = \frac{2-\alpha_{\mathrm{p}}}{\alpha_{\mathrm{p}}}\sqrt{\pi}\nu\beta\frac{\partial u_0}{\partial y} + \frac{1}{5}\frac{k}{nk_{\mathrm{b}}}\frac{1}{T}\frac{\partial T}{\partial x}, \tag{2.34}$$

using the definition of λ from equation (1.5)

$$\lambda = \nu\sqrt{\frac{\pi M}{2k_{\mathrm{b}}T}} = \sqrt{\pi}\nu\beta, \tag{2.35}$$

and the following relation between k and μ from Shen [5]

$$k = \frac{15}{4}\frac{k_{\mathrm{b}}}{M}\mu, \tag{2.36}$$

the velocity at the surface can be given by

$$u_{\mathrm{s}} = \lambda\frac{\partial u_0}{\partial y} + \frac{3}{4}\nu\frac{1}{T}\frac{\partial T}{\partial x} = C_{\mathrm{p}}\lambda\frac{\partial u_0}{\partial y} + K_{\mathrm{tc}}\nu\frac{1}{T}\frac{\partial T}{\partial x}. \tag{2.37}$$

This relatively simple model gives $C_{\mathrm{p}} = 1.0$ and $K_{\mathrm{tc}} = \frac{3}{4}$. The first term, the slip term, vanishes in the limit $\lambda \to 0$. The second term, the thermal creep term, does not vanish in the continuum limit and means that the gas has a velocity component relative to the wall in the direction of the temperature gradient. This implies a force on the gas from the wall in the direction of the temperature gradient, and thereby a force on the wall from the gas in the opposite direction, which is the cause of the thermophoretic force. The expression for the temperature jump can be derived in a similar way

$$T_{\mathrm{w}} = \left(\frac{2-\alpha_{\mathrm{e}}}{\alpha_{\mathrm{e}}}\right)\lambda \mathrm{C}_{\mathrm{e}}\frac{\partial T}{\partial y}. \tag{2.38}$$

More sophisticated models give more accurate values of C_{p},K_{tc} and C_{e}, than obtained by this method. Averages based on different models (see Young [10]) are given in table 2.1.

Table 2.1: Different parameters for the boundary conditions at a solid wall taken from Young [10].

Parameter	Value
C_e	2.17
C_p	1.13
K_{tc}	1.10

Given the boundary conditions the thermophoretic force on the particle can be found in the slip flow regime. Brock's [17] solution from 1963 can be given in non-dimensional form as

$$\Phi = \frac{-12\pi K_{tc}(1 + \Lambda C_e Kn)}{(1 + 3C_p Kn)(2 + \Lambda + 2\Lambda C_e Kn)}, \tag{2.39}$$

where $\Lambda = \frac{k_p}{k_{gas}}$ is the ratio of the thermal conductivities between the particle and the gas and Φ is the non-dimensional thermophoretic force defined as

$$\boldsymbol{F}_{th} = \Phi Kn \frac{\mu^2 r_p^2 \nabla T}{\lambda \rho T} = \Phi \frac{\mu^2 r_p \nabla T}{\rho T}, \tag{2.40}$$

where $\boldsymbol{F}_{th}$ is the thermophoretic force, r_p the particle radius and μ, ρ and T is the dynamic viscosity, density and temperature for the undisturbed gas. It is assumed that the particles will not influence the fluid flow significantly for more than one mean free path length away from the particle. This solution is intended for the near continuum regime, but Talbot et al. [9] discovered that by adjusting C_p and K_{tc} slightly the expression in the limit $Kn \to \infty$ was in good agreement with the Waldmann limit. The expression from Talbot et al. has been widely used for practical calculations.

Young [10] incorporates results from numerical simulations in an interpolation formula for practical calculations which can be used for all Knudsen numbers. It is based on the Grad 13-moment method and numerical solutions by Yamamoto and Ishihara [18] and Bresenev and Chernyak [19], where the latter is preferred. The thermophoretic force in dimensionless form is then given by

$$\Phi = \frac{-12\pi[K_{tc}(1 + \Lambda C_e Kn) + 3C_p Kn(1 - \Lambda + \Lambda C_e Kn)]}{(1 + 3Kn\ e^{-C_{int}/Kn})(1 + 3C_p Kn)(2 + \Lambda + 2\Lambda C_e Kn)}, \tag{2.41}$$

where C_{int} is an interpolation constant. A choice of $C_{int} = 0.5$ is used as recommended by Young [10]. The dimensionless thermophoretic force for various Knudsen numbers and thermal conductivities is shown in fig 2.2.

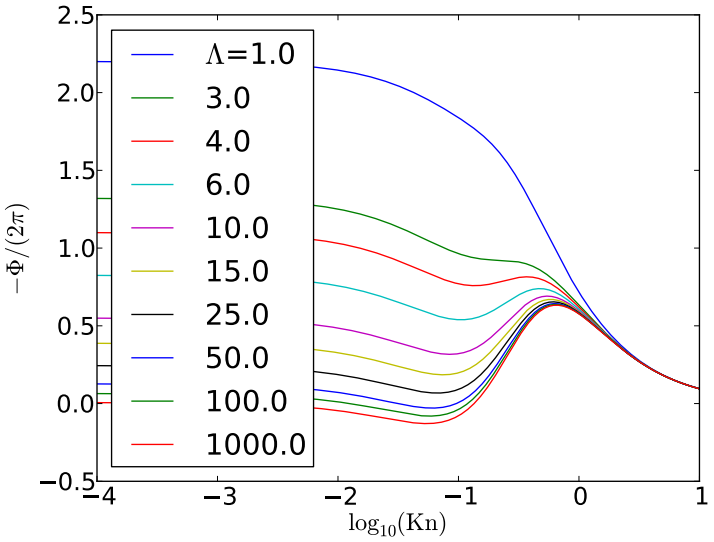

Figure 2.2: The thermophoretic force in dimensionless form

2.2.2 The drag force

The drag force on a particle, $\boldsymbol{F}_\mathrm{D}$, with velocity $\boldsymbol{v}$ in a fluid with velocity $\boldsymbol{u}$ is given by

$$\boldsymbol{F}_\mathrm{D} = \frac{1}{2}\rho \mathrm{C}_\mathrm{D} A|\boldsymbol{u}-\boldsymbol{v}|(\boldsymbol{u}-\boldsymbol{v})/\mathrm{C}_\mathrm{c} = \frac{1}{2}\rho \mathrm{C}_\mathrm{D} A|\boldsymbol{u}_\mathrm{rel}|\boldsymbol{u}_\mathrm{rel}/\mathrm{C}_\mathrm{c}, \tag{2.42}$$

where $A = \pi r_p^2$ is the cross section of a particle with radius r_p. If the particle Reynolds number, $\mathrm{Re}_\mathrm{p} = 2r_\mathrm{p}\frac{|\boldsymbol{u}_\mathrm{rel}|}{\nu}$ is less than 1000, the drag coefficient C_D is given by

$$\mathrm{C}_\mathrm{D} = \frac{24}{\mathrm{Re}_\mathrm{p}}(1 + 0.15\mathrm{Re}_\mathrm{p}^{0.687}). \tag{2.43}$$

When the particles are small continuum fluid mechanics must be corrected as mentioned earlier, in the case of drag this is done by introducing the Stokes-Cunningham factor,

$$\mathrm{C}_\mathrm{c} = 1 + \mathrm{Kn}\left(1.257 + 0.4e^{-1.1\mathrm{Kn}}\right). \tag{2.44}$$

The drag force can be written in a compact form as

$$\boldsymbol{F}_\mathrm{D} = \frac{m_\mathrm{p}}{\tau_\mathrm{p}}\boldsymbol{u}_\mathrm{rel}, \tag{2.45}$$

where m_p is the mass of the particle and τ_p is the particle response time given by

$$\tau_\mathrm{p} = \frac{2m_\mathrm{p}\mathrm{C_c}}{\rho \mathrm{C_D}\pi r_\mathrm{p}^2 |\boldsymbol{u}_\mathrm{rel}|} = \frac{\mathrm{S}d_\mathrm{p}^2\mathrm{C_c}}{18\nu(1+0.15\mathrm{Re_p^{0.687}})}, \tag{2.46}$$

where $\mathrm{S} = \frac{\rho_\mathrm{p}}{\rho}$, ρ_p is the particle mass density and d_p is the particle diameter.

A measure of the particle response to drag is the Stokes number, St, which is defined as the ratio between the particle response time, τ_p, and the fluid time scale, τ_f,

$$\mathrm{St} = \frac{\tau_\mathrm{p}}{\tau_\mathrm{f}}. \tag{2.47}$$

2.2.3 Thermophoretic velocity

Given a steady flow with constant temperature, density and viscosity the drag force will eventually balance out the thermophoretic force and the particle will have a constant velocity relative to the fluid, the thermophoretic velocity $\boldsymbol{v}_\mathrm{th}$. Using equation (2.40) and (2.45) the following expression can be obtained

$$\begin{aligned}
\boldsymbol{v}_\mathrm{th} &= \Phi\frac{\mu^2 r_\mathrm{p}\nabla T}{\rho T}\cdot\frac{\tau_\mathrm{p}}{m_\mathrm{p}} \\
&= \Phi\frac{\mu^2 r_\mathrm{p}\nabla T}{\rho T}\cdot\frac{\mathrm{S}(2r_\mathrm{p})^2 C_\mathrm{c}}{18\nu(1+0.15\mathrm{Re_p}^{0.687})}\cdot\frac{1}{\frac{4}{3}\pi\rho_\mathrm{p}r_\mathrm{p}^3} \\
&= \Phi\frac{3\mu C_\mathrm{c}\nabla T}{18\pi\rho T(1+0.15\mathrm{Re_p^{0.687}})}.
\end{aligned} \tag{2.48}$$

It has to be noted that $\mathrm{Re_p}$ will depend on the thermophoretic velocity. However if it is assumed that $\mathrm{Re_p} \approx 0$ is valid, the thermophoretic velocity reduces to

$$\boldsymbol{v}_\mathrm{th} = \Phi C_\mathrm{c}\frac{\nu\nabla T}{6\pi T}, \tag{2.49}$$

and a non-dimensional thermophoretic velocity, Ψ, can be defined as

$$\Psi = \frac{\boldsymbol{v}_\mathrm{th}\cdot T}{\nu\nabla T} = \frac{\Phi C_\mathrm{c}}{6\pi}. \tag{2.50}$$

In figure 2.3, Ψ has been plotted in for various Λ. The thermophoretic velocity is often the quantity measured when measuring the thermophoretic force in experimental set-ups. The thermophoretic force and the drag force depend upon quantities like temperature, velocity, density, viscosity and temperature gradient of the gas, these quantities are determined by the fluid equations described in section 2.1, since the particles in general are not exactly located

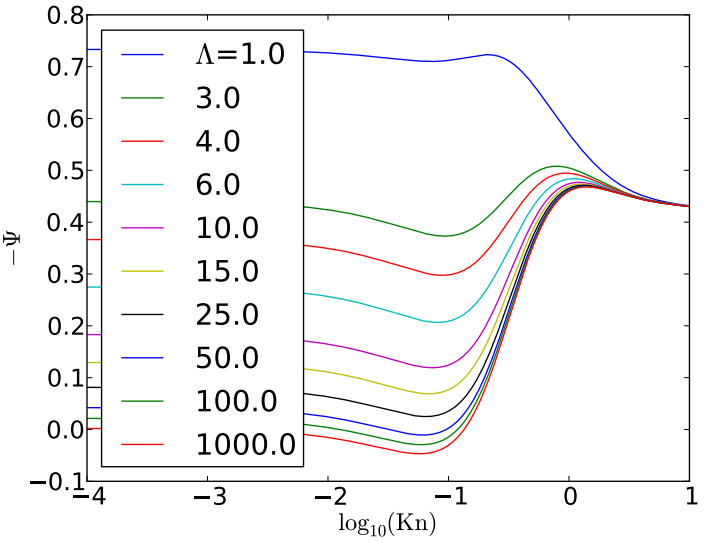

Figure 2.3: The thermophoretic velocity in dimensionless form.

at a grid point interpolation is required. In the following a first order interpolation scheme is used for density, temperature and velocity and for the temperature gradient a nearest grid point interpolation is used.
.

Chapter 3

Numerical method

In order to solve the particle and fluid equations a numerical method is required. When the Navier-Stokes equations are solved with Direct Numerical Simulation an efficient code is needed because it is very costly even for relatively small Reynolds numbers. The code used is The Pencil Code [15] which calculates the fluid field and based on this the force on the particles. The parameter values used in the simulations can be found in appendix A.

3.1 The Pencil Code

The Pencil Code is a high-order finite-difference code for compressible hydrodynamic flows written in FORTRAN90. The code runs efficiently under MPI on massively parallel shared- or distributed-memory computers, like e.g. large Beowulf clusters. The Pencil Code is named after its use of pencils, which means that quantities like density and velocity is calculated along one dimension at the time for each time step, this is done to ensure that all the memory required by the CPU is available in the computers cache.

3.1.1 Discretization

There are many methods for discretization of differential equations. The methods used in this project and implemented in The Pencil Code is the finite-difference method in space and Runge-Kutta in time. The finite-difference method is based on approximating the spatial derivatives with finite differences. The order of the method corresponds to the accuracy of the method i.e. a sixth order method, which is used in this context with a grid spacing of Δx has an error of $\mathcal{O}(\Delta x^6)$. In order to approximate the derivative of a quantity at a grid point i six neighbour points are required $(i-3,\, i-2,\, i-1,\, i+1,\, i+2,\, i+3)$ for a sixth order method. The sixth

order first derivative scheme used in The Pencil Code [15] is given by

$$\frac{\partial g_i}{\partial x} = \frac{-g_{i-3} + 9g_{i-2} - 45g_{i+1} - 9g_{i+2} + g_{i+3}}{60\Delta x}. \tag{3.1}$$

The discretization used in time is an explicit Runge-Kutta method of third order. The Runge-Kutta method is based on successive iterations starting with the solution from the explicit Euler method. A partial differential equation (PDE), can be transformed to an ordinary differential equation (ODE) by discretisizing in the spatial direction, thus obtaining a semi discrete differential equation. Consider the simple PDE

$$\frac{\partial g}{\partial t} = \frac{\partial g}{\partial x}, \tag{3.2}$$

the right hand term can be discretisized according to equation (3.1) and be denoted as $R(g,t)$

$$\frac{\partial g}{\partial t} = R(g,t), \tag{3.3}$$

then the explicit Euler method can be used to discretisize in time

$$g_1(t+\Delta t) = g_1(t) + \Delta t \cdot \mathrm{R}(g(t),t). \tag{3.4}$$

The i-th order Runge-Kutta is then given by

$$g_i(t+\Delta t) = \alpha_i g_{i-1}(t) + \Delta \mathrm{t} \cdot \mathrm{R}(g_{i-1}(t), t_{i-1}) \tag{3.5}$$

where α_i is a constant. The 3rd order Runge-Kutta method used in this study is therefore of order $\mathcal{O}(\Delta t^3)$.

For a numerical method to be meaningful it is required to be consistent, i.e. that when $\Delta x \to 0$, $\Delta t \to 0$ the error of the numerical method vanishes, in addition the method must be stable. When these criteria are fulfilled the method is convergent by the Lax equivalence theorem, also called the Lax-Richtmeyer equivalence theorem, as in Strikwerda [20].

3.1.2 Stability conditions

As mentioned above an absolute criteria for the numerical method is stability. The stability condition is determined by the Courant-Friedrichs-Lewy (CFL) condition which states that the time step must be smaller than the time information uses to travel one grid length, the CFL time step will then be the smallest of the convective and diffusive time step:

$$\Delta t = \min\left(c_{\Delta t}\frac{\Delta x_{\min}}{U_{\max}}, c_{\Delta t,\mathrm{v}}\frac{\Delta x_{\min}^2}{D_{\max}}\right) \tag{3.6}$$

where $c_{\Delta t}$ and $c_{\Delta t,\mathrm{v}}$ are the CFL numbers and

$$\Delta x_{\min} \equiv \min(\Delta x, \Delta y) \tag{3.7}$$

$$U_{\max} \equiv \max\left(|\mathbf{u}| + c_{\mathrm{s}}\right) \tag{3.8}$$

$$D_{\max} = \max(\nu, \gamma\chi) \tag{3.9}$$

c_{s} is the speed of sound. In addition the time step must be smaller than the particle response time determined by equation (2.46). Because the computing cost increases with decreasing time step it is desirable to have a high Mach number (low speed of sound), $\mathrm{Ma} = \frac{u_0}{c_{\mathrm{s}}}$, but not too high because of compressible effects.

3.1.3 The solid geometry

Solid objects, like in this case a cylinder, have to be included in the flow domain. To make the code general a Cartesian grid has been used, which does not follow the boundary of the cylinder. This requires a modification of the equations close to the boundary. The method used in this study is the immersed boundary method, which adds a virtual force to the momentum equation (2.11) to make sure the boundary conditions are fulfilled. The method was first introduced by Peskin to study the flow around heart valves [21] and now refers to a class of methods for simulations of flow around boundaries on non-body-conformal grid, for an overview see Mittal and Iaccarino [22].

There are in principle no restrictions on the choice of the virtual forcing as long as the boundary conditions are met. The method used in this study is the discrete forcing approach where the equations are first discretisized on a Cartesian grid and then the forcing is introduced. This approach allows direct control over the numerical accuracy, stability and discrete conservation properties of the solver.

In order to accurately resolve the boundary layer ghost points are used within the solid body. Values are assigned to the ghost points based on the properties of their mirror points in the fluid ensuring a sharp wall between the fluid and the solid. The mirror points are found by identifying the surface normal. Because of the curvature of the boundary the mirror point of a grid point inside the cylinder will not always coincide with a grid point in the fluid, then interpolation of the four nearest neighbours is required. If the grid point is too close to the cylinder to have four neighbours in the fluid an interpolation is made along the surface normal between the surface and the point where the surface normal intersects its first grid line inside the fluid. The state of the latter point is found by a linear interpolation of the closest grid points along the grid line.

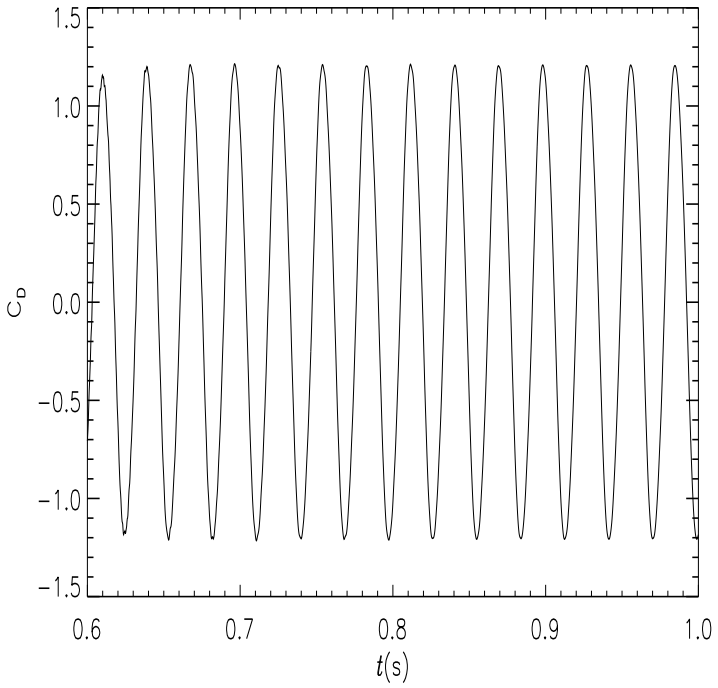

Figure 3.1: The oscillations of the drag coefficient in y-direction when the flow field is statistical stationary.

When the fluid points are too close to the boundary spurious effects may arise due to the effective delocalized dependency in the finite differences. Since calculating the central sixth-order finite difference requires the use of ghost points given by mirror points relatively far from the original point. To avoid spurious effects a pre-defined cut-off is chosen (e.g. $0.7\ \Delta x$), such that if the grid point is closer than this to the boundary a value is assign explicitly based on the same procedure as described in the previous paragraph.

In the stream wise direction partial reflecting Navier-Stokes characteristic boundary conditions (NSCBC) have been used for the fluid. The particles are inserted a few grid points down stream and removed at the outlet. For the fluid and the particles periodic boundary conditions are used in the span wise direction.

3.2 The particles

There will take some time before the numerical solution of the flow field is statistical stationary and the Von Kármán eddies form behind the cylinder.

Therefore a simulation without particles was performed first to initialise the flow field. When the flow field was statistically stationary the particles were inserted. In figure 3.1 the drag coefficient of the cylinder is shown when the flow field was stationary. Because of the oscillations caused by the Von Kármán the particles was inserted over a time of at least three Von Kármán periods in order to achieve good statistics. The initial velocity of the particles was set equal to the fluid velocity. And the initial positions of the particles in the span-wise direction were uniformly distributed in a range such that they span the cylinder diameter. The particles was removed at the outlet and if they impacted on the cylinder, and the simulation was run until no particles remained.

Chapter 4

The non-isothermal reference cases

In this chapter the results for the simulations without thermophoresis will be presented and discussed. The results consist of isothermal and non-isothermal cases at Re = 20 and Re = 380. In the non-isothermal case the free stream temperature, T_0, and the cylinder temperature, T_c, was set to: $T_0 = 873$ K and $T_c = 700$ K. In the Re = 20 case a grid size of 1024×512 was used and in the Re = 380 case a grid size of 2048×1024 was used. The case with Re = 20 is stationary and less computationally demanding than the case with Re = 380, and was therefore performed to determine the differences between isothermal and non-isothermal flow.

Table 4.1: The front side impaction efficiency for the non-isothermal case, η_{front}, and for the isothermal case, $\tilde{\eta}_{\text{front}}$, for different Stokes numbers and Re = 20.

St	η_{front}	$\tilde{\eta}_{\text{front}}$	$\eta_{\text{front}}/\tilde{\eta}_{\text{front}}$
0.05	0.000227	0.000183	1.24
0.10	0.000421	0.000397	1.06
0.15	0.000685	0.000634	1.08
0.30	0.002329	0.001757	1.33
1.00	0.257760	0.632461	1.19
3.00	0.632461	0.616187	1.03
10.00	0.902221	0.894426	1.10

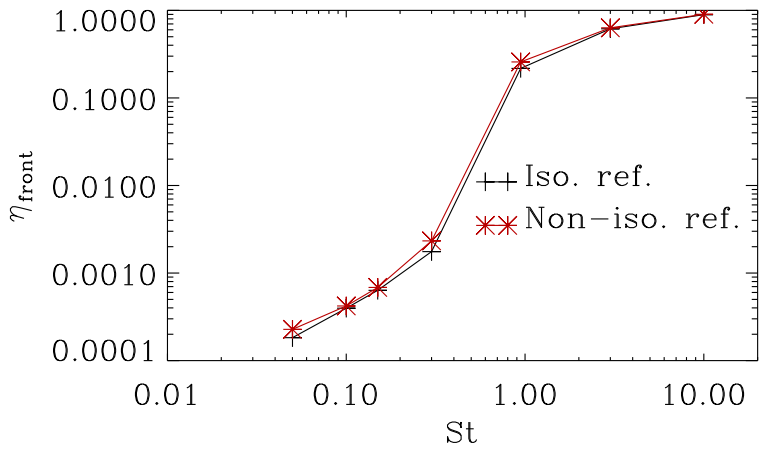

Figure 4.1: The front side particle impaction efficiency for non-isothermal and isothermal flow for Re = 20.

4.1 Low Reynolds number simulations

The front side impaction efficiencies for the isothermal and non-isothermal case for simulations with Re= 20 are shown in figure 4.1. The front side impaction efficiencies and the ratio between the non-isothermal and the isothermal front side impaction efficiencies are given in table 4.1. The results show slightly larger impaction efficiency for the non-isothermal case compared to the non-isothermal case for all Stokes numbers considered.

Haugen and Kragset [2] identified three modes of impaction depending on the Reynolds number and the Stokes number. The particles with the largest Stokes numbers, St > 0.7 for Re $= 20$, experience classical impaction. The particles have sufficient inertia to penetrate the boundary layer in this mode. In the boundary stopping mode the particles no longer penetrates the boundary layer, this mode exists for $0.3 <$ St < 0.7 for Re $= 20$. For Stokes numbers below this the particles experience boundary interception; i.e. the particles follow the flow perfectly. One must keep in mind that the Stokes number depends on the viscosity, St $\sim \frac{1}{\mu}$, which is temperature dependent. In the non-isothermal case the viscosity decreases as the temperature decreases towards the cylinder, meaning that the particles resist the flow better than indicated by the free stream Stokes number. This effect would explain the higher impaction efficiency in the non-isothermal compared to the isothermal case. The free stream Stokes number should therefore be replaced by an effective Stokes number, but since the effective Stokes number would depend

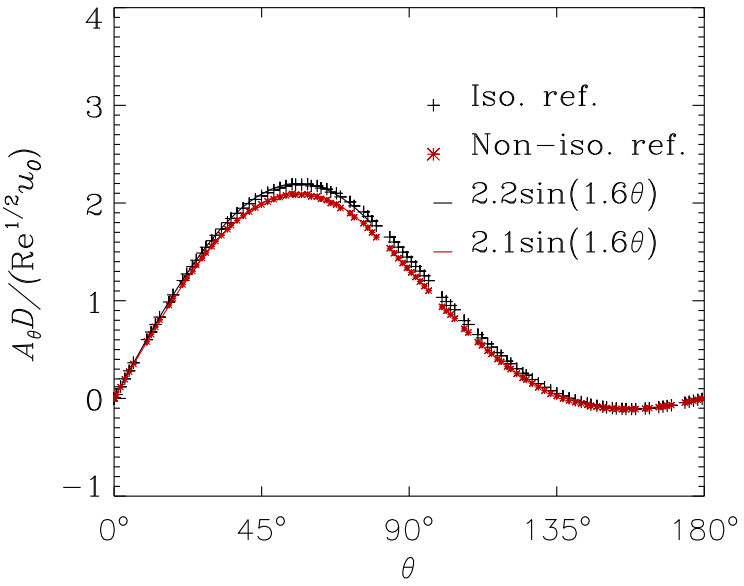

Figure 4.2: The isothermal and the non-isothermal show the same angular dependence of $1/B_\theta$ and the maximum value is almost the same.

on how much time the particles spend in the boundary layer it would be very complicated to find.

In the boundary interception mode the particles follow the flow perfectly, but still impact due to the finite extent of the particles. Haugen and Kragset [2] gave an expression for the front side impaction efficiency as a function of Stokes number in the boundary interception mode. In this section a similar expression will be derived for the non-isothermal case. For the Reynolds number considered the boundary layer will be laminar and the tangential velocity in the boundary layer can be assumed linear

$$u_\theta = A_\theta \hat{x}, \tag{4.1}$$

where A_θ is a constant depending on the Reynolds number, $\hat{x}$ is the normal distance from the surface. The angle θ is 0° at the front side and increasing clockwise around the cylinder. For the isothermal case Haugen and Kragset [2] used the following expression for the boundary layer thickness

$$\delta = \frac{B_\theta D}{\sqrt{\mathrm{Re}}} \tag{4.2}$$

to find

$$A_\theta = \frac{u_0\sqrt{\mathrm{Re}}}{B_\theta D}, \tag{4.3}$$

where $1/B_\theta$ is a Reynolds number independent constant. The skin friction coefficient is defined in White [23] as

$$\mathrm{C_f} = \frac{\tau}{\frac{1}{2}\rho u_0^2}, \tag{4.4}$$

where τ is the shear stress at the wall. In this case

$$\tau = \mu\frac{\partial u_\theta}{\partial \hat{x}} = \mu A_\theta, \tag{4.5}$$

which implies that

$$\mathrm{C_f} = \frac{2\nu A_\theta}{u_0} = \frac{2}{\sqrt{\mathrm{Re}}}\frac{1}{B_\theta}, \tag{4.6}$$

or

$$\frac{1}{B_\theta} = \frac{\mathrm{C_f}}{2}\sqrt{\mathrm{Re}}. \tag{4.7}$$

In the isothermal case Haugen and Kragset [2] measured A_θ and fitted a sine to the values of $1/B_\theta$ for various Reynolds numbers with a best fit of

$$\tilde{f} = 2.2\,\sin(1.6\theta), \tag{4.8}$$

in the range $0° < \theta < 80°$. In figure 4.2, $1/B_\theta$ have been plotted for the isothermal and non-isothermal case for Re$=$ 20. The results for the isothermal case are in excellent agreement with equation (4.8) while the non-isothermal results fit better with a fit of

$$f(\theta) = 2.1\,\sin(1.6\theta). \tag{4.9}$$

The difference between the cases is only 5% and they show the same angular dependence. Using equation (4.9) the tangential velocity can be expressed as

$$u_\theta = \alpha f(\theta), \tag{4.10}$$

where

$$\alpha = \frac{u_0\sqrt{\mathrm{Re}}}{D}. \tag{4.11}$$

The difference between the isothermal and non-isothermal case can be explained by looking at the viscous term in the Navier-Stokes equation (2.11),

$$\frac{1}{\rho}\nabla\cdot(2\mu\mathbf{S}) = 2\nu\nabla\cdot\mathbf{S} + \frac{2\mathbf{S}}{\rho}\cdot\nabla\mu, \tag{4.12}$$

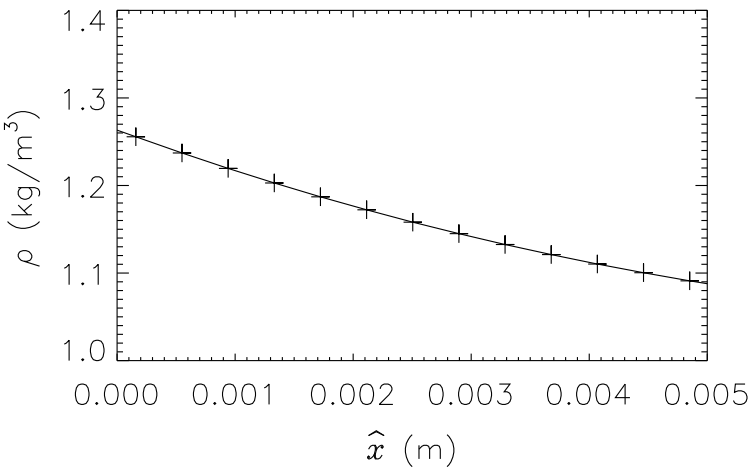

Figure 4.3: The density, ρ, as a function of distance from the cylinder $\hat{x}$ at $\theta = 0°$

both ν and μ decreases as the temperature decreases towards the cylinder. If only the first term is considered a decrease in ν corresponds to an increase in the Reynolds number giving a thinner boundary layer. While the second term will be directed away from the cylinder giving a thicker boundary layer. In this case since the isothermal, $\tilde{f}$, is slightly higher than the non-isothermal, f, the net result is a thicker boundary layer in the non-isothermal case.

The continuity equation (2.8) can be written in cylindrical coordinates in two-dimensions as

$$u_{\mathrm{r}}\frac{\partial \rho}{\partial r} + \frac{u_\theta}{r}\frac{\partial \rho}{\partial \theta} = -\rho\frac{\partial u_r}{\partial r} - \frac{1}{r}\rho\frac{\partial u_\theta}{\partial \theta}, \tag{4.13}$$

where r is the distance from the center of the cylinder. Since the density gradients are caused by the temperature gradients and the temperature gradients close to the cylinder can be assumed to only have a radial component it can be deduced that $\frac{\partial \rho}{\partial \theta} \approx 0$. Requiring the boundary layer to be thin compared to the radius R_{c} of the cylinder reduces the equation to

$$\begin{aligned} u_r\frac{\partial \rho}{\partial \hat{x}} + \rho\frac{\partial u_r}{\partial \hat{x}} &= -\frac{\rho}{R_{\mathrm{c}}}\frac{\partial u_\theta}{\partial \theta}, \\ \frac{\partial \rho u_{\mathrm{r}}}{\partial \hat{x}} &= -\frac{\rho}{R_{\mathrm{c}}}\frac{\partial u_\theta}{\partial \theta}, \end{aligned} \tag{4.14}$$

where $\hat{x}$ is the distance from the cylinder surface. The density as a function of distance from the cylinder from the non-isothermal simulation is shown in

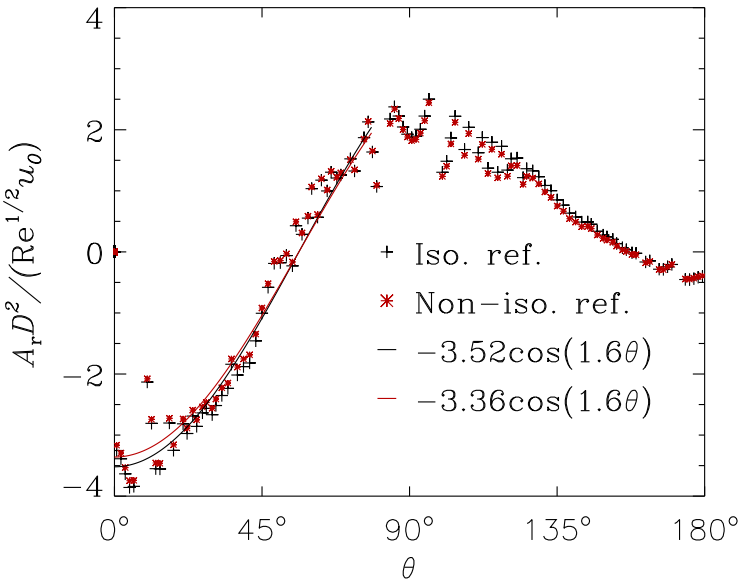

Figure 4.4: The isothermal and non-isothermal $1/B_\mathrm{r}$ is essentially the same.

figure 4.3. The density close to the cylinder can be approximated by

$$\rho = \rho_\mathrm{c} - \xi \cdot \hat{x}, \tag{4.15}$$

where ρ_c is the density at the cylinder surface and ξ is the density gradient close to the cylinder. Numerical estimates can be obtained from the figure 4.3 giving $\rho_\mathrm{c} = 1.26$ kg/m^3 and $\xi = 44.44$ kg/m^4. The estimate for ρ_c agrees well with the ideal gas law, which gives $\rho_\mathrm{c} = \rho \cdot \frac{T_0}{T_\mathrm{c}} \approx 1.25$ kg/m^3. Using equation (4.14) and (4.15), an expression for the radial velocity can be found

$$u_\mathrm{r} = -\frac{1}{\rho}\int_0^{\hat{x}} \frac{\rho}{R_\mathrm{c}}\frac{\partial u_\theta}{\partial \theta}\mathrm{d}\hat{x}' = -\frac{1}{\rho R_\mathrm{c}}\alpha\hat{x}^2\frac{\partial f}{\partial \theta}\left(\frac{1}{2}\rho_\mathrm{c} - \frac{1}{3}\xi\hat{x}\right), \tag{4.16}$$

equation (4.15) implies that $\rho_\mathrm{c} = \rho + \xi\cdot\hat{x}$, inserting this in the above equation yields

$$u_\mathrm{r} = -\frac{1}{2R_\mathrm{c}}\alpha\hat{x}^2\frac{\partial f}{\partial \theta}\left(1 + \frac{1}{3}\frac{\xi\hat{x}}{\rho}\right). \tag{4.17}$$

Comparing with the isothermal radial velocity, $\hat{u}_\mathrm{r}$, from Haugen and Kragset [2] gives

$$u_\mathrm{r} = \hat{u}_\mathrm{r}\left(1 + \frac{1}{3}\frac{\xi\hat{x}}{\rho}\right), \tag{4.18}$$

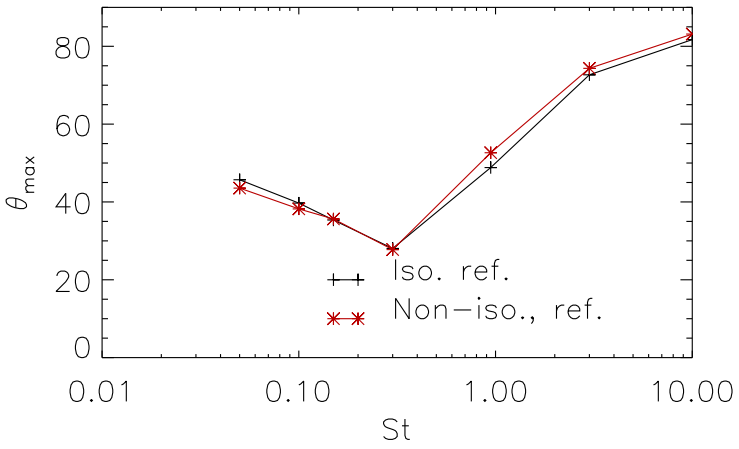

Figure 4.5: The maximum angle of front side impaction, $\theta_{\max}$ as function of Stokes number for isothermal and non-isothermal flow for Re = 20.

in the very close boundary layer the second term can be neglected, the radial velocity will then be proportional to the square of the distance from the surface i.e.

$$u_{\mathrm{r}} = A_{\mathrm{r}}\hat{x}^2, \tag{4.19}$$

where

$$A_{\mathrm{r}} = -\frac{\alpha}{D}\frac{\partial f}{\partial \theta} = \frac{\alpha}{D}\frac{1}{B_{\mathrm{r}}}, \tag{4.20}$$

which implies

$$\frac{1}{B_{\mathrm{r}}} = -\frac{\partial f}{\partial \theta} = -3.36\,\cos(1.6\theta). \tag{4.21}$$

For small angles, i.e. close to the front side stagnation point, the radial velocity will be directed towards the cylinder surface. When $\frac{\partial f}{\partial \theta} = 0$ the boundary layer is at its thinnest and from this point onwards the radial velocity will be directed away from the surface. A particle which has not impacted at this point will not impact on the front side at all, by using equation (4.21) this is found to happen at $\theta \approx 56°$. In figure 4.4, $1/B_{\mathrm{r}}$ has been plotted for the isothermal and non-isothermal case, both agree well with the expected results and the radial velocity become zero at the same angle for the two cases. This is reflected in figure 4.5, where the maximum angle of impaction for the two cases are plotted as a function of Stokes number.

The total mass flow in the boundary layer between the cylinder surface

and one particle radius away from the surface is

$$\begin{aligned}\dot{m}_{\mathrm{b}} = H\int_0^{r_{\mathrm{p}}} \rho u_\theta \mathrm{d}\hat{x}^{'} &= H\alpha f(\theta)\left(\frac{1}{2}\rho_{\mathrm{c}} r_{\mathrm{p}}^2 - \frac{1}{3}\xi r_{\mathrm{p}}^3\right), \\ &= \frac{1}{2}H\alpha f(\theta) r_{\mathrm{p}}^2 \rho_{\mathrm{c}}\left(1 - \frac{2}{3}\frac{\xi r_{\mathrm{p}}}{\rho_c}\right),\end{aligned} \tag{4.22}$$

where H is the length of the cylinder. The total mass flow inserted between the axis and Δy away from the axis far upstream is

$$\dot{m}_{\mathrm{u}} = H u_0 \rho_0 \Delta y, \tag{4.23}$$

by setting $\dot{m}_{\mathrm{u}} = \max(\dot{m}_{\mathrm{b}})$, the following expression is obtained

$$\eta = \frac{\Delta y}{r_{\mathrm{c}}} = \frac{\sqrt{\mathrm{Re}}}{4}\left(\frac{r_{\mathrm{p}}}{r_{\mathrm{c}}}\right)^2 f_{\max}\frac{\rho_{\mathrm{c}}}{\rho_0}\left(1 - \frac{2}{3}\frac{\xi r_{\mathrm{p}}}{\rho_{\mathrm{c}}}\right), \tag{4.24}$$

by using the ideal gas law and assuming $\frac{\xi r_{\mathrm{p}}}{\rho_{\mathrm{c}}} \approx 0$ the following expression is obtained

$$\eta \approx \frac{\sqrt{\mathrm{Re}}}{4}\left(\frac{r_{\mathrm{p}}}{r_{\mathrm{c}}}\right)^2 f_{\max}\frac{T_0}{T_{\mathrm{c}}}. \tag{4.25}$$

Comparison with the isothermal expression, $\tilde{\eta}$, from Haugen and Kragset gives

$$\eta = \tilde{\eta}\frac{f_{\max}}{\tilde{f}_{\max}}\frac{T_0}{T_{\mathrm{c}}}. \tag{4.26}$$

Inserting the numerical values for $f_{\max}$, $\tilde{f}_{\max}$, T_0 and T_{c} yields

$$\eta = \tilde{\eta}\cdot\frac{2.1}{2.2}\cdot\frac{873}{700} \approx 1.19\cdot\tilde{\eta}. \tag{4.27}$$

This equation was derived assuming the particles follow the stream perfectly, which means $\mathrm{St} = 0$. No finite particles follow the stream perfectly, but the results of the impaction efficiencies from the simulations is in good agreement with equation (4.27) for $\mathrm{St} = 0.05$. This indicates that equation (4.27) is valid for the interception mode.

The simulations at $\mathrm{Re} = 20$ have shown that the front side impaction efficiency in the non-isothermal case is slightly higher than in the isothermal case. The dominating effect behind this for the small Stokes numbers was found to be that the higher density close to the cylinder leads to a higher mass flow in the non-isothermal case compared to the isothermal case. Meaning that a streamline Δy away from the center-line in the non-isothermal case is closer to the cylinder surface than the corresponding streamline in the isothermal case.

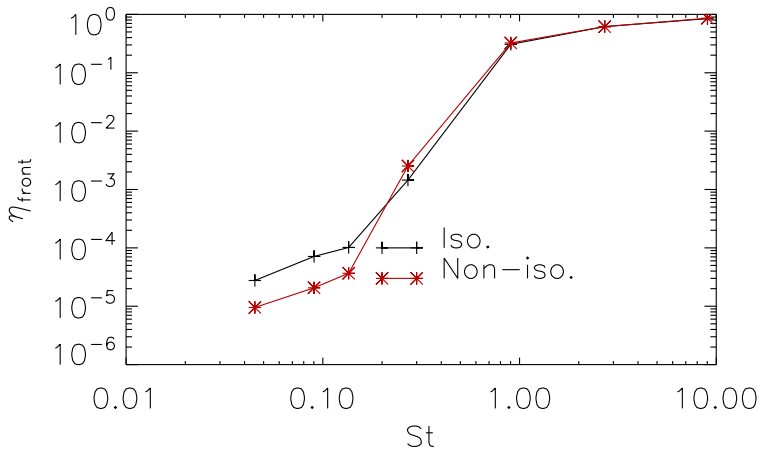

Figure 4.6: The front side particle impaction efficiency for isothermal and non-isothermal flow for Re = 380.

4.2 Intermediate Reynolds number simulations

The front side impaction efficiencies for the non-isothermal and isothermal cases with Re = 380 are shown in figure 4.6. In contrast to what was found in the previous section the impaction efficiency for the three smallest Stokes numbers was considerable lower in the non-isothermal case compared to the isothermal case. The smallest particles are very sensitive to the very close boundary layer. For Re = 380 the flow is non-stationary, in order to plot $1/B_\theta$ and $1/B_\mathrm{r}$ the average of the velocity above and below the cylinder is taken, such that $\bar{u}_\theta(\theta) = \frac{1}{2}(u_\theta(\theta) - u_\theta(2\pi - \theta))$ and correspondingly for u_r. The plot of $1/B_\theta$ in figure 4.7 shows no considerable differences between the isothermal and non-isothermal reference case at least not larger than was found for Re = 20. The plot of $1/B_\mathrm{r}$ in figure 4.8, however shows large variations in $1/B_\mathrm{r}$ for the non-isothermal case, and positive values of $1/B_\mathrm{r}$ even for small angles. These variations suggest that the lower impaction efficiency in the non-isothermal compared to the isothermal case is a result of errors in the numerical method. The smallest particles are most sensitive to the close boundary layer and is probably the explanation to why only the smallest particles are affected by the numerical errors.

Haugen and Kragset [2] performed grid independence tests and found for Re = 421 that a grid size of 1024×512 was sufficient for isothermal flow. Since a grid size of 2048×1024 still gives problems in the non-isothermal case, it is unlikely that a further increase of the grid size will improve the

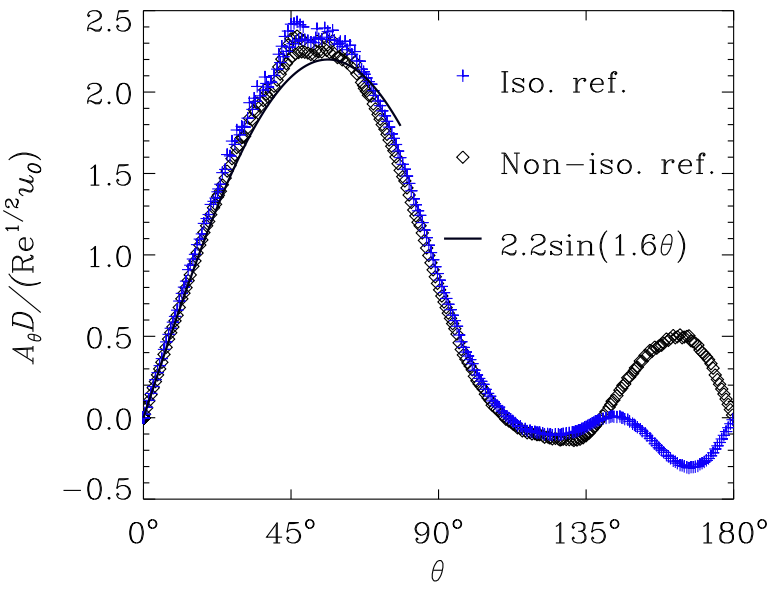

Figure 4.7: The Reynolds-number-independent constant $1/B_\theta$ as a function of the angle θ. Both the isothermal and the non-isothermal case, with $T_\mathrm{c} = 700$ K, agrees well with the fit from equation (4.8). The close_linear_limit parameter is set to $l = 0.7$ for both cases.

situation.

Close to the cylinder interpolation is required to avoid spurious effects caused by delocalization of the numerical method, as described in chapter 3. The cut-off, close_linear_limit, determining how close a fluid point must be to the cylinder surface before interpolation is required was originally set to $l = 0.7$. Which means that if a grid point is closer to the cylinder surface than $0.7{\cdot}\Delta x$ the value of that grid point is interpolated. The parameter l was varied and the results for $1/B_\theta$ and $1/B_\mathrm{r}$ are shown in figure 4.9 and figure 4.10 respectively. Increasing l does improve the situation for the radial velocities close to the front side stagnation point, but it causes problems around 40°. In the non-isothermal case it is difficult to find a value of l, which yields satisfactory results. Possible solutions to this problem could be to use a higher order interpolation scheme, using a one-sided stencil for calculating derivatives close to the cylinder surface or using a body-conformal grid.

The current method uses only the two nearest grid points when calculating the values for grid points close to the cylinder, extending the method to using

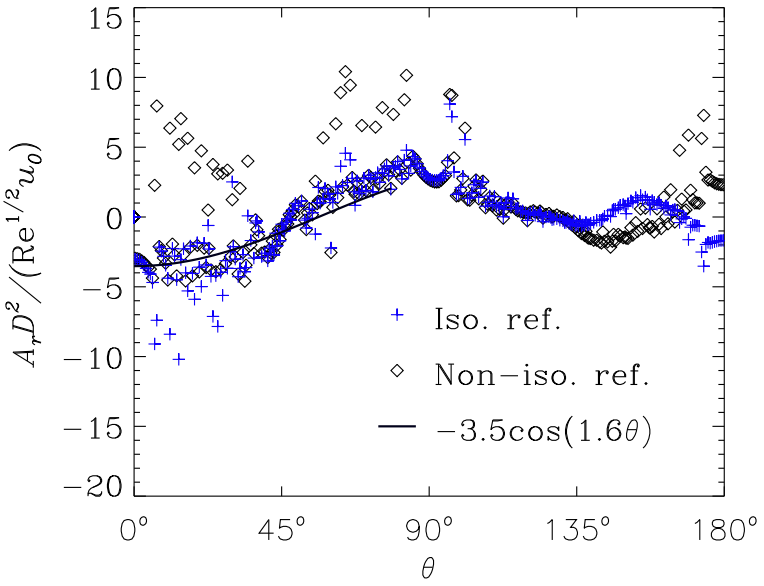

Figure 4.8: The Reynolds-number-independent constant $1/B_\mathrm{r}$ as a function of the angle θ. The non-isothermal case, has positive values for the radial velocity close to the front side stagnation point, which does not agree with the fit from equation (4.21) and the isothermal case. The close_linear_limit parameter is set to $l = 0.7$ for both cases.

the four nearest neighbours instead would be desirable. Achieving higher order interpolation could be rather complicated as one must be sure that the grid points used for interpolation are fluid points. The interpolation could be eliminated altogether by solving the problem with delocalization by using a one-sided stencil for calculating derivatives close to the cylinder. Instead of calculating the derivatives using three grid points on either side one could have an uneven distribution using e.g. 4 points to the left and two points to the right and thus avoid using more than one ghost points within the cylinder when calculating derivatives. The last option is to use a body-conformal grid instead of the immersed boundary method, using a body-conformal grid will make it easier to implement the boundary conditions, but it is in general difficult to generate the grid and it would make the code less general. All of these methods will require substantial amount of time to implement, which would require more time than the time frame of this study. With knowledge of the boundary layer for different choices of l and with the considerations done for low Reynolds number as background, the effect of the numerical

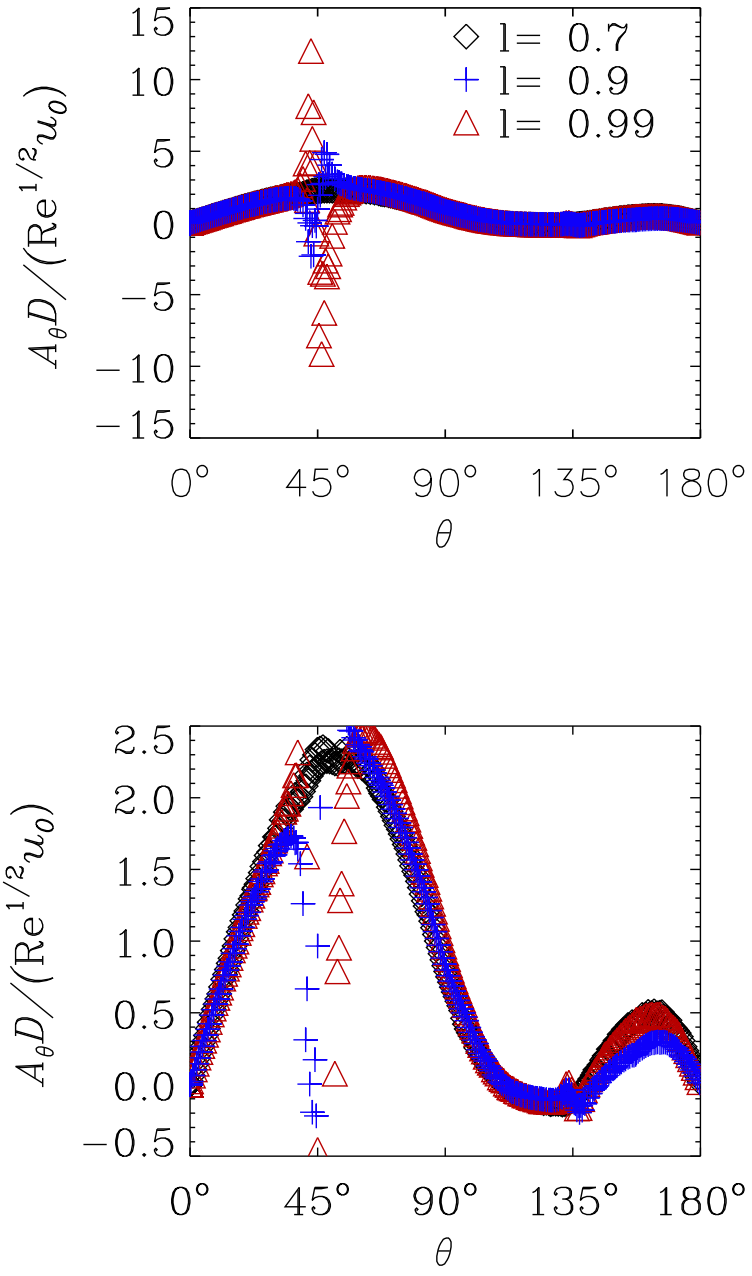

Figure 4.9: Variation of the interpolation parameter l gives different results for $1/B_\theta$ in the non-isothermal case, $\mathrm{Re} = 380$.

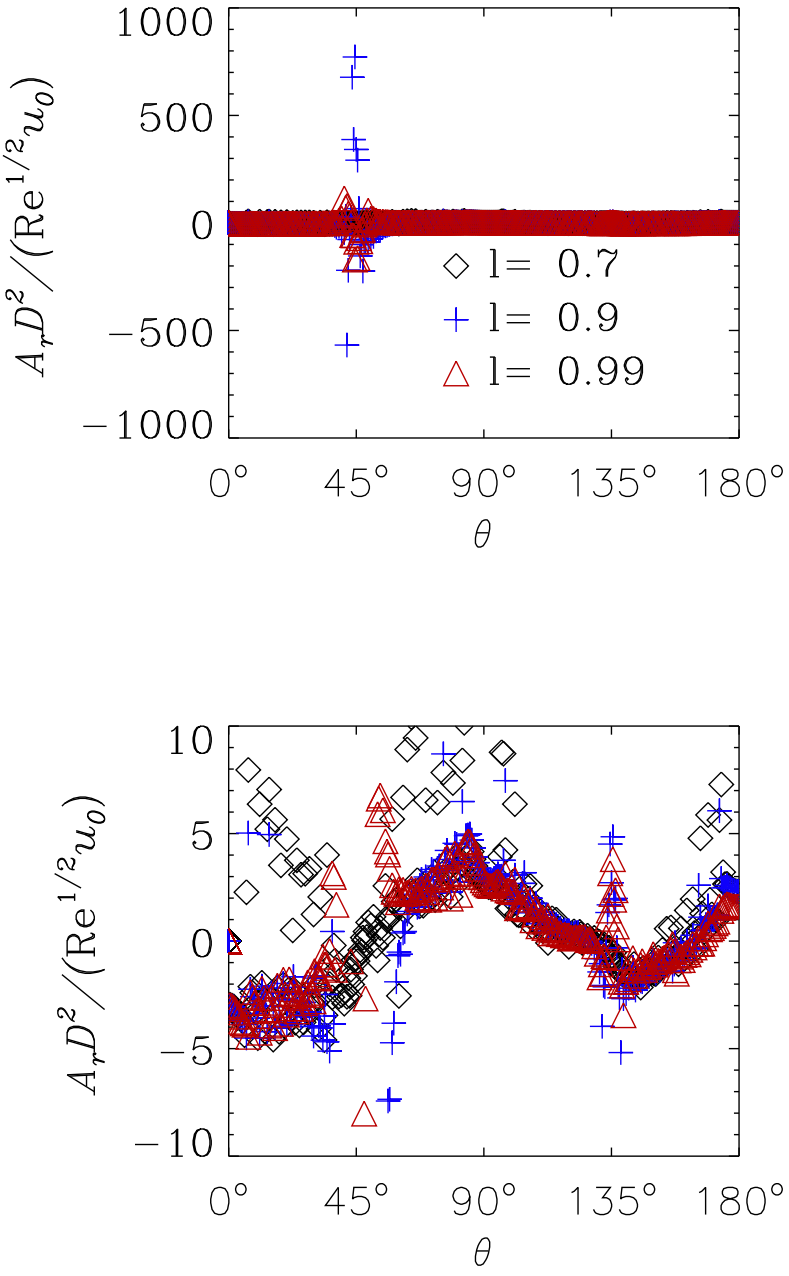

Figure 4.10: Variation of the interpolation parameter l gives different results for $1/B_\mathrm{r}$ in the non-isothermal case, $\mathrm{Re} = 380$.

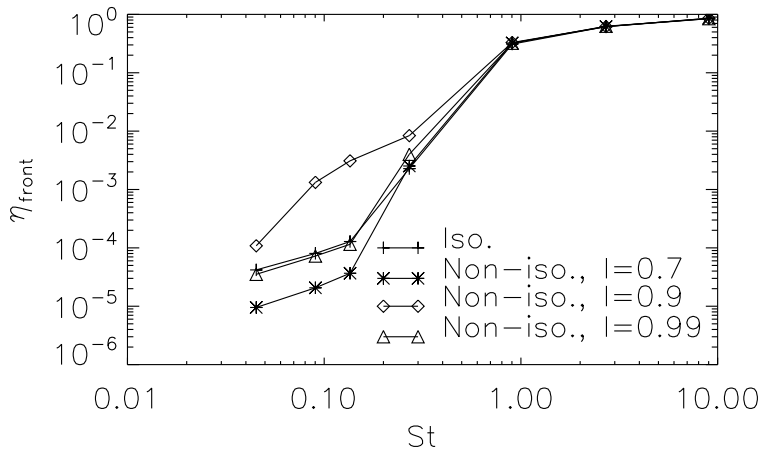

Figure 4.11: Front side impaction efficiency as function of Stokes numbers for the isothermal case and for the non-isothermal cases with different values of the limit_close_linear parameter, l, for Re = 380.

errors on the particle impaction can be discussed. A comparison between the front side impaction efficiencies for the non-isothermal cases and the isothermal case is shown in figure 4.11, and a similar comparison for the maximum angle of impaction is shown in figure 4.12.

The non-isothermal case with $l = 0.7$ has positive radial velocities for small angles and the maximum angle of impaction is therefore only $\theta_{\max} \approx 10°$ for the smallest Stokes numbers. For the two other cases the radial velocities are either strongly negative and then strongly positive, $l = 0.9$, or the opposite for $l = 0.99$. If the radial velocity is strongly negative many of the particles which had not impacted will impact, while if the radial velocity is positive the particles do not impact. In the previous section it was found for Re = 20 that the maximum angle of impaction for the isothermal and non-isothermal case was more or less the same. If it is assumed that the same holds for Re = 380 one can deduce that a strong positive radial velocity at $\theta \approx 40°$ will have little effect on the front side particle impaction for the small Stokes numbers considered in this case, because the maximum angle of impaction in the isothermal case is below 40°.

For Re = 380 the choice of $l = 0.99$ gives the most accurate results for the front side particle impaction in the non-isothermal case. Since $1/B_\theta$ and $1/B_r$ is in good agreement with the isothermal case for $\theta < 40°$, and since the inaccuracies at $\theta \approx 40°$ repel the particles rather than attracting them.

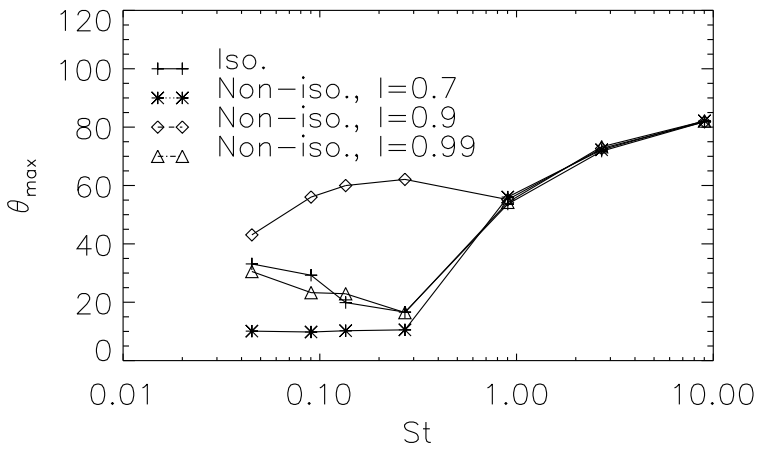

Figure 4.12: Maximum angle of front side impaction, $\theta_{\max}$, as a function of Stokes number for the isothermal case and for the non-isothermal cases with different values of the limit_close_linear parameter, l, for Re = 380.

4.2.1 Back side impaction

Because of the Von Kármán eddies formed behind the cylinder for Re $>$ $\mathrm{Re}_{\mathrm{Kármán}}$ there is particle impaction on the back side even when the drag force from the gas is the only force on the particles considered. If the eddy turnover time is long enough for the particle to gain momentum in the direction opposite of the free stream direction and short enough for the particle to escape the eddy, then the particle might impact on the back side.

The back side impaction efficiency for Re = 380 is shown in figure 4.13. There were only back side impaction for the three smallest Stokes numbers. The mechanisms behind back side impaction are much more complicated than for the front side impaction and there is difficult to explain the differences between the different non-isothermal cases and the isothermal case.

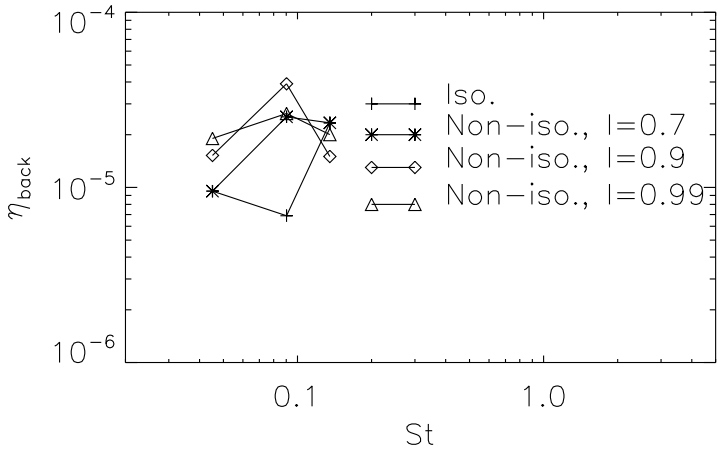

Figure 4.13: The back side impaction efficiency as function of Stokes numbers for the isothermal case and for non-isothermal cases for different values of the limit_close_linear parameter, l, for Re = 380

Chapter 5

Thermophoresis

In this chapter the results from the simulations with thermophoresis will be presented and discussed. In the range of particle sizes considered the thermophoretic force depends on the particle-to-gas thermal conductivity ratio, $\Lambda = \frac{k_p}{k_{gas}}$. The values of Λ chosen in this study are 1, 100 and 1000. A Reynolds number of Re = 380 has been used. Since $l = 0.99$ gave the best results for the non-isothermal reference case this value has been used in the thermophoretic cases.

5.1 The front side impaction

The front side impaction efficiency is shown in figure 5.1, and the ratio between the front side impaction efficiencies for the cases with thermophoresis and the front side impaction efficiency for the non-isothermal reference case are given in table 5.1. For St $\gtrsim$ 1.0, there are no substantial differ-

Table 5.1: The ratio between the front side impaction efficiency with thermophoresis and without thermophoresis for different Stokes numbers and values of Λ.

St	$\Lambda = 1$	$\Lambda = 100$	$\Lambda = 1000$
0.05	205.999	7.288	0.000
0.10	127.679	5.169	0.111
0.15	104.619	5.269	0.520
0.30	9.790	2.386	0.871
1.00	1.017	0.992	1.014
3.00	0.999	0.988	0.998
10.00	1.012	0.987	1.012

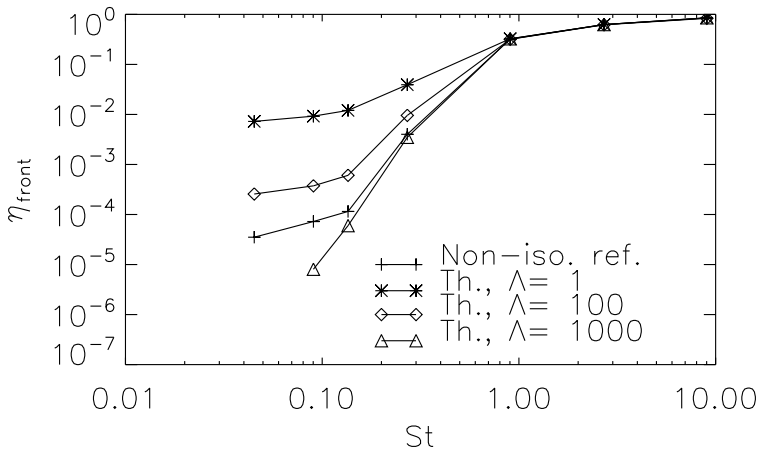

Figure 5.1: The front side impaction efficiency for the non-isothermal case as function of Stokes numbers with and without thermophoresis for different values of Λ

ences in the impaction efficiency of the non-isothermal reference case and the thermophoretic cases. These particles experience classical impaction, they penetrate the boundary layer and are therefore not affected much by thermophoresis. For $\mathrm{St} \lesssim 1.0$ thermophoresis affects the particle impaction efficiency depending on Λ.

The particle impaction efficiency is presented as a function of Stokes number, while the thermophoretic force was presented in terms of the Knudsen number in chapter 2. Using equation (1.2) and (2.47), and assuming $C_\mathrm{c} \approx 1$ and $\mathrm{Re_p} \approx 0$, the relation between the Knudsen number and the Stokes number for a particle can be found as

$$\mathrm{Kn_p} = \lambda \sqrt{\frac{4 \cdot \mathrm{S} \cdot u_0}{9 \cdot \mathrm{St} \cdot \nu \cdot D}} = \frac{1}{3} \mathrm{Kn_c} \sqrt{\frac{\mathrm{Re} \cdot \mathrm{S}}{\mathrm{St}}}, \tag{5.1}$$

where $\mathrm{Kn_c}$ is the cylinder Knudsen number $\mathrm{Kn_c} = \frac{\lambda}{R_\mathrm{c}}$. Inserting numerical values for the case considered gives

$$\mathrm{Kn_p} = 8.17 \cdot 10^{-4} \cdot \frac{1}{\sqrt{\mathrm{St}}}, \tag{5.2}$$

the Knudsen numbers for the particles considered in this case is therefore in the range $2.58 \cdot 10^{-4} < \mathrm{Kn_p} < 8.17 \cdot 10^{-3}$. The Stokes number in terms of

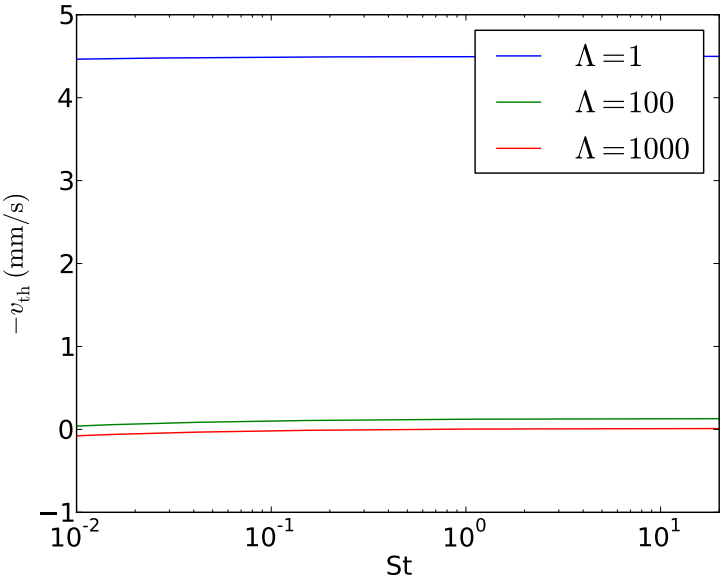

Figure 5.2: The thermophoretic velocity as a function of Stokes number for different values of Λ.

the Knudsen number then becomes

$$\mathrm{St} = 6.68 \cdot 10^{-7} \cdot \frac{1}{\mathrm{Kn}_\mathrm{p}^2}. \tag{5.3}$$

Using this relation and the expression for the thermophoretic velocity (2.48), v_{th} can be expressed in terms of the Stokes number. In figure 5.2, v_{th} has been plotted as a function of Stokes number for the values of Λ used in the simulations, when representative values of ν, T and ∇T have been inserted.

The relative small values of the thermophoretic velocity, in the order of mm/s, affects the impaction efficiencies significantly. This can be explained by considering that the smallest particles are of the order of 10 μm and the particles impacting on the cylinder can spend relatively long time in the close boundary layer.

The cases with $\Lambda = 1$ and $\Lambda = 100$ give higher impaction as the thermophoretic force is directed towards the cylinder. The impaction efficiency in the thermophoretic case is for $\Lambda = 100$ and $\Lambda = 1$ respectively, almost one order and two orders of magnitude greater than the impaction efficiency in the reference case for the smallest Stokes numbers considered. While the case with $\Lambda = 1000$ gives lower impaction for the smallest Stokes numbers and for $\mathrm{St} = 0.05$ no front side impaction was found at all.

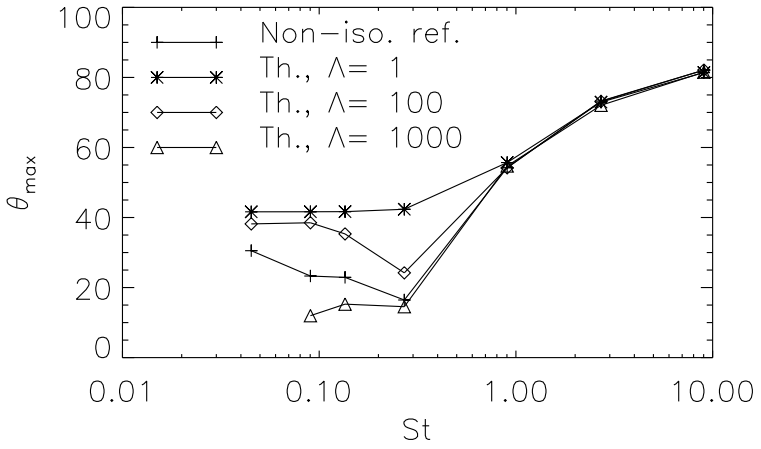

Figure 5.3: The maximum angle of front side impaction as a function of Stokes number for the non-isothermal case with and without thermophoresis for different values of Λ

The parameters Kn and Λ are in general temperature dependent since they depend on the fluid quantities λ and k_{gas} respectively, but in these simulations they have been held constant. Since the temperature decreases towards the cylinder λ decreases towards the cylinder. The value of the Knudsen number should therefore be lower close to the cylinder compared to the free stream value, likewise Λ should be higher close to the cylinder compared to the free stream values. Using temperature dependent Kn and Λ would give some minor corrections to the particle impaction efficiency.

The maximum angle of front side impaction is affected by thermophoresis as well, the cases with $\Lambda = 1$ and $\Lambda = 100$ give a higher $\theta_{\max}$ than the non-isothermal reference case. They both reach a maximum value of $\theta_{\max} \approx 40°$, it is likely that this is an effect of the numerical inaccuracies for the non-isothermal case in this region as discussed in the previous chapter. For the case $\Lambda = 1000$ the maximum angle of impaction is lower than in the reference case.

In the case without thermophoresis analytical considerations was made regarding the small Stokes number impaction, in this subsection a similar approach will be used for the thermophoretic case. It will be assumed that the particles reach equilibrium between the thermophoretic force and the drag force instantaneously, the particle velocity in the radial direction can then be given as the sum of the radial velocity of the fluid and of the thermophoretic

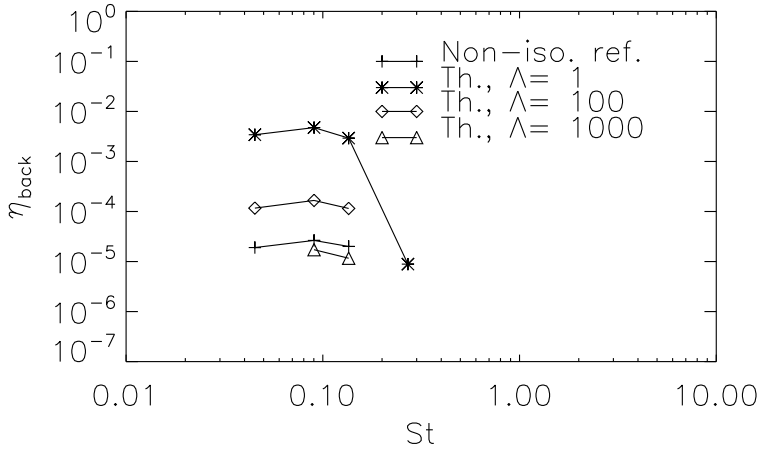

Figure 5.4: The back side impaction efficiency for the non-isothermal case as function of Stokes numbers with and without thermophoresis for different values of Λ

velocity

$$\dot{\hat{x}} = A_{\mathrm{r}} \cdot \hat{x}^2 + v_{\mathrm{th}}, \tag{5.4}$$

inserting the expression for A_{r} gives

$$\dot{\hat{x}} = -3.5\frac{\alpha}{D}\cos(1.6\theta) \cdot \hat{x}^2 + v_{\mathrm{th}}, \tag{5.5}$$

without thermophoresis the maximum angle of impaction was found when the first term became positive, but with thermophoresis the maximum angle of impaction takes place either at a higher angle, if $v_{\mathrm{th}} < 0$, or at a lower angle, if $v_{\mathrm{th}} > 0$.

5.2 Back side impaction

The back side impaction efficiency is shown in figure 5.4. The ratio between the back side impaction efficiencies for the cases with thermophoresis and the non-isothermal reference case is given in table 5.2. It is seen that thermophoresis leads to a considerable increase for $\Lambda = 1$ and $\Lambda = 100$ compared to the non-isothermal reference case. For $\Lambda = 1$ back side impaction was found even for St $= 0.3$. The back side impaction efficiency in the thermophoretic case with $\Lambda = 1000$ was slightly lower than in the non-isothermal reference case and no back side impaction was found for St $= 0.05$.

Table 5.2: The ratio between the back side impaction efficiency with thermophoresis and without thermophoresis.

St	$\Lambda = 1$	$\Lambda = 100$	$\Lambda = 1000$
0.05	179.986	6.142	0.000
0.10	179.910	6.297	0.652
0.15	146.192	5.743	0.582

5.3 The effect of thermophoresis

In this study only particles with $0.05 < \mathrm{St} < 10$ have been considered, however based on the expression of the thermophoretic force and the results for the Stokes numbers considered some considerations can be made for the general case. It was found that thermophoresis has little effect on the impaction efficiency for $\mathrm{St} \gtrsim 1$, therefore particle impaction for higher Stokes number than those considered will essentially be unaffected by thermophoresis.

Since $\theta_{\max}$ for the cases with $\Lambda = 1$ and $\Lambda = 100$ probably were affected by the numerical inaccuracies, it is likely that the effect of thermophoresis on the front side particle impaction efficiency is even higher than what was found in these simulations. In the thermophoretic case with $\Lambda = 1$ the inaccuracies around 40° probably had little effect on the front side impaction efficiency, but the implementation of temperature dependent Λ and Kn on the other hand can have a substantial effect. Since for this value of Λ the particles experience negative thermophoresis for some of the Stokes numbers. If the Knudsen number of the particle is shifted then the onset of negative thermophoresis might occur for a different Stokes number.

It is difficult to say what effect the numerical inaccuracies have on the back side impaction, because if the number of particles impacting on the front side is decreased there are more particles reaching the back side of the cylinder. On the other hand the inaccuracies may deflect particles that otherwise would have impacted on the back side.

Although the numerical method used in this study should be improved in the non-isothermal case, the simulations performed give valuable information about the effect of thermophoresis. It is clear that thermophoresis have a considerable effect on the front side particle impaction. The impaction efficiency for $\mathrm{St} \lesssim 1.0$ was found to be material dependent, for low particle conductivities it was substantially increased and for high particle conductivities it was decreased. In appendix B values of Λ used in different experimental studies can be found. For much lower Stokes numbers than those considered in this study the impaction efficiency is expected to be material independent, since the thermophoretic force is material independent in the free molecule limit.

5.4 Further work

The focus of further work should be to improve the method to eliminate the numerical inaccuracies for non-isothermal flows at intermediate Reynolds numbers. When this has been done the effect of thermophoresis on the particle deposition at other Reynolds numbers than $\mathrm{Re} = 380$ should be studied, since the Reynolds number considered in this study does not necessarily represent the real situationin a heat exchanger. The temperature of the incoming gas and of the cylinder may be different as well, which may have an effect both on the fluid flow and on the thermophoretic force. Brownian motion will not be specifically directed towards the cylinder as thermophoresis, but can still be important for the particle deposition and future work should consider this effect as well.

The incoming flow is not necessarily laminar, if the flow is turbulent the temperature distribution around the cylinder will be different from the laminar case. The thermophoretic force will then not necessarily be directed towards the cylinder. Another aspect of turbulent non-isothermal flow is Turbulent Thermal Diffusion (TTD) a phenomenon described theoretically by Elperin, Kleeorin and Rogachevskii in 1996 [24]. TTD also gives a force on the particle towards the cylinder, but has different origins then thermophoresis.

The simulations have shown that the smallest particles are very sensitive to the thermophoretic force. Therefore accurate knowledge of the thermophoretic force on the particles is needed in order to describe the particle impaction for the smallest particles. Very little experimental data on thermophoresis on particles with the Knudsen numbers considered in this work exist, this is especially the case for high particle conductivities where it is unclear if negative thermophoresis exists. Further it was assumed spherical particles, mono atomic gas and no rotation of the particles, in general this can not be assumed to hold.

Conclusion

The effect of thermophoresis on the particle deposition on a cooled cylinder in non-isothermal laminar gas flow has been studied with Direct Numerical Simulation using the immersed boundary method with ghost points; for Re $= 380$, $\frac{T_c}{T_0} = 700/873$, particle-to-gas thermal conductivity ratios $\Lambda = 1, 100, 1000$ and Stokes numbers in the range $0.01 <$ St < 10. In addition to the simulations where thermophoresis were taken into account two reference simulations have been performed; an isothermal reference case and a non-isothermal reference case. To verify the fluid implementation for non-isothermal flow an isothermal and a non-isothermal reference case for Re $= 20$ was performed.

Analytical considerations found that the ratio between the front side impaction efficiencies for the smallest particles in the non-isothermal and isothermal reference case was proportional to $\frac{T_0}{T_c}$, which agreed well with the simulations for Re $= 20$, but not for Re $= 380$. The reason to this is believed to be inaccuracies in the numerical method for the non-isothermal simulation at Re $= 380$.

It was found that thermophoresis does not affect the particle impaction for St $\gtrsim 1.0$, for St $\lesssim 1.0$ the effect of thermophoresis depended on Λ. Both the front side and back side particle impaction efficiency was significantly higher for the thermophoretic cases with $\Lambda = 1$ and $\Lambda = 100$ than for the non-isothermal reference case. For $\Lambda = 1000$ lower particle impaction efficiency was found in the thermophoretic case compared to the non-isothermal reference case both for the front side and the back side.

For the Stokes/Knudsen numbers considered in this study the thermophoretic force on the particles is material dependent and therefore the impaction efficiency will be material dependent for the Stokes numbers where thermophoresis has an effect. For much smaller particles than those considered in this study the thermophoretic force will no longer be material dependent.

Appendix A

Parameter values

All simulations

The computational domain

Length of domain:	$L_\mathrm{x} = 0.4$ m, $L_\mathrm{y} = 0.2$ m
Radius of cylinder:	$R_\mathrm{c} = 0.01685$ m
Position of cylinder at the center of the domain:	$x = 0.2$ m, $y = 0.0$ m

Particles

Insertion width:	$w_\mathrm{par} = 2 \cdot R_\mathrm{c}$
Number of particles inserted:	$N = 3 \cdot 10^6$
Insert rate:	$r_\mathrm{insert} = 3.325 \cdot 10^7$ s^{-1}
Stokes numbers:	St = 0.05, 0.10
	0.15, 0.30
	1.00, 3.00, 10.00
Initial velocity of particles:	$u_\mathrm{x} = 5.0$ m/s
Particle density:	$\rho_\mathrm{p} = 1000.0$ kg/m^3

Miscellaneous

Mean free path gas:	$\lambda = 67.0$ nm
Gas density at inlet:	$\rho_0 = 1.0$ kg/m^3
Velocity of incoming flow:	$u_0 = 5.0$ m/s

Re = 20

Particle radii:	r_p (μm) = 79.95, 113.04, 138.42
	195.78, 347.47, 619.11, 1130.37

Isothermal case

Speed of sound	$c_\mathrm{s} = 40.0$ m/s
Kinematic viscosity:	$\nu = 0.00843$ m^2/s
limit_close_linear:	$l = 0.7$

Non-isothermal case

Thermal conductivity at inlet:	$k_0 = 0.03371$ W/(m $\cdot$ K)
Kinematic viscosity at inlet:	$\nu_0 = 0.00843$ m^2/s
Inlet temperature:	$T_0 = 873.0$ K
Cylinder temperature:	$T_\mathrm{c} = 700.0$K
Specific heat capacity at constant pressure:	$c_\mathrm{p} = 4.0$ J/(kg $\cdot$ K)
Prandtl number:	Pr $= 1.0$
limit_close_linear:	$l = 0.7$

Re = 380

Particle radii:	r_p (μm) = 17.42, 24.63, 30.16 42.66, 77.89, 134.90, 246.30

Isothermal case

Speed of sound	$c_\mathrm{s} = 40.0$ m/s
Kinematic viscosity:	$\nu = 0.00044$ m^2/s
limit_close_linear:	$l = 0.7$

Non-isothermal case

Thermal conductivity at inlet:	$k_0 = 0.00177$ W/(m $\cdot$ K)
Kinematic viscosity at inlet:	$\nu_0 = 0.00044$ m^2/s
Inlet temperature:	$T_0 = 873.0$ K
Cylinder temperature	$T_\mathrm{c} = 700.0$ K
Specific heat capacity at constant pressure:	$c_\mathrm{p} = 4.0$ J/(kg $\cdot$ K)
Prandtl number:	Pr $= 1.0$
Particle-to-gas thermal conductivity:	$\Lambda = 1$, 100, 1000
limitclose_linear, reference case	$l_\mathrm{ref} = 0.7$, 0.9, 0.99
limit_close_linear, thermophoretic cases	$l_\mathrm{th} = 0.99$

Appendix B

Particle-to-gas thermal conductivity ratio for various particles and gases

Particle and gas	Λ[1]
TCP in air	10
NaCl in air	309 -322
PMMA in air	7.9
SiO_2 in air	74
Wax in air	4.6
PSL in air	5.4
Ag in air	22530
Vegetable oil in air	10
Castor oil in air	9.5
Silicone oil in air	7.5
TCP in air	10
Hg in air	581
DOP in air	6
Glass in air	40
Ni in air	4700
Al in He	1519
DOP in He	0.8
NaCl in Ar	300
Cork in Ar	2.5
PSL in CO_2	10
DOP in CO_2	12
Glass in CO_2	75

[1] Taken from table 2 and 3 in Young [10]

Bibliography

[1] R. Israel and D. E. Rosner. Use of a generalized stokes number to determine the aerodynamic capture efficiency of non-stokesian particles from a compressible gas flow. *Aerosol Science and Technology*, 2(1):45–51, 1982.

[2] N. E. L. Haugen and S. Kragset. Particle impaction on a cylinder in a crossflow as function of stokes and reynolds numbers. *Journal of Fluid Mechanics*, 661:239–261, 2010.

[3] J. Tyndall. On dust and disease. *Proc. R. Inst.*, 6:1–14, 1870.

[4] J. Aitken. On the formation of small clear spaces in dusty air. *Trans. R. Soc. Edinb.*, 32:239–272, 1884.

[5] C. Shen. *Rarefied Gas Dynamics*. Springer, 2005.

[6] F. Zheng. Thermophoresis of spherical and non-spherical particles: a review of theories and experiments. *Advances in Colloid and Interface Science*, 97(1-3):255 – 278, 2002.

[7] P. S. Epstein. Zur theorie des radiometers. *Zeitschrift für Physik*, 54(7-8):537–563, 1929.

[8] L. Waldmann. Über doe Kraft eines inhomogenen Gases auf kleine suspendierte Kugeln. *Zeitschrift Naturforschung Teil A*, 14:589, July 1959.

[9] L. Talbot, Cheng, R. W. Schefer, and D. R. Willis. Thermophoresis of particles in a heated boundary layer. *Journal of Fluid Mechanics*, 101(04):737–758, 1980.

[10] J. B. Young. Thermophoresis of a spherical particle: Reassessment, clarification, and new analysis. *Aerosol Science and Technology*, 45(8):927–948, 2011.

[11] C. Shen. Thermophoretic deposition of particles onto cold surfaces of bodies in two-dimensional and axisymmetric flows. *Journal of Colloid and Interface Science*, 127(1):104 – 115, 1989.

[12] M. C. Chiou and J. W. Cleaver. Effect of thermophoresis on sub-micron particle deposition from a laminar forced convection boundary layer flow onto an isothermal cylinder. *Journal of Aerosol Science*, 27(8):1155 – 1167, 1996.

[13] M. C. Chiou, C. H. Chiu, and H. S. Chen. Modeling particle deposition from fully developed turbulent flow. *Applied Mathematical Modelling*, 35(7):3238 – 3254, 2011.

[14] C. H. K. Williamson. Vortex dynamics in the cylinder wake. *Annual Review of Fluid Mechanics*, 28:477–539, 1996.

[15] W. Dobler and A. Brandenburg. The pencil code, manual. www.nordita.org/software/pencil-code.

[16] S. Chapman and T. G. Cowling. *The mathematical theory of non-uniform gases: an account of the kinetic theory of viscosity, thermal conduction and diffusion in gases.* Cambridge University Press, 3. edition, 1970.

[17] J. R. Brock. On the theory of thermal forces acting on aerosol particles. *Journal of Colloid Science*, 17(8):768 – 780, 1962.

[18] K. Yamamoto and Y. Ishihara. Thermophoresis of a spherical particle in a rarefied gas of a transition regime. *Physics of Fluids*, 31(12):3618–3624, 1988.

[19] S. Beresnev and V. Chernyak. Thermophoresis of a spherical particle in a rarefied gas - Numerical analysis based on the model kinetic equations. *Physics of fluids*, 7(7):1743–1756, JUL 1995.

[20] J. C. Strikwerda. *Finite Differences and Partial Differential Equations.* Chapman & Hall, 1. edition, 1989.

[21] C. S. Peskin. The immersed boundary method. *Acta Numerica*, 11:479–517, 2002.

[22] R. Mittal and G. Iaccarino. Immersed boundary methods. *Annual Review of Fluid Mechanics*, 37(1):239–261, 2005.

[23] F. M. White. *Viscous Fluid Flow.* McGraw Hill, 3. edition, 2006.

[24] T. Elperin, N. Kleeorin, and I. Rogachevskii. Turbulent thermal diffusion of small inertial particles. *Phys. Rev. Lett.*, 76:224–227, Jan 1996.